Evidence for a composite organic–inorganic fabric of belemnite rostra

Elsevier Editorial System(tm) for Sedimentary Geology

Manuscript Draft

Manuscript Number: SEDGEO5702R1

Title: Evidence for a composite organic-inorganic fabric of belemnite rostra: Implications for palaeoceanography and palaeoecology

Article Type: Research Paper

Keywords: belemnite, ultrastructure, carbonate archive, diagenesis, Jurassic-Cretaceous

Corresponding Author: Dr. Rene Hoffmann,

Corresponding Author's Institution: Ruhr Universität Bochum

First Author: Rene Hoffmann

Order of Authors: Rene Hoffmann; D. K. Richter; R. D. Neuser; N. Jöns; Linzmeier B. J.; R. E. Lemanis; F. Fusseis; X. Xiao; A. Immenhauser

Abstract: Carbonate skeletons of fossil marine organisms are widely used to reconstruct palaeoceanographic parameters. Specifically, the geochemistry of Jurassic and Cretaceous belemnite rostra is traditionally interpreted to represent near sea-surface seawater properties. More recently, an increasing number of workers, have reported significant scatter in geochemical data (e.g., δ18O, δ13C, element/Ca ratio) when comparing rostra from the same stratigraphic level or within a single belemnite rostrum. This scatter is not explained by differential diagenetic overprint alone. Here we report petrographic evidence on the primary ultrastructure of rostra of Megateuthis (Middle Jurassic) and Belemnitella and Gonioteuthis (Late Cretaceous). The biogenic ultrastructure consists of a filigree framework of triaxial branches and tetrahedrons of variable size forming a honeycomb-like network. Data presented here suggest that these rostra yielded as much as 50 to 90% primary pore space. On the level of a working hypothesis - and in analogy with modern cephalopods - we propose that the pore space was formerly filled with body fluid and/or organic compounds during the life time of these organisms. Intra-rostral porosity was post mortem occluded by earliest diagenetic isopachous calcite cements of a non-biogenic origin. These may have been precipitated due to increased alkalinity related to the decay of organic matter. If this holds true, then the resulting fabric represents a composite biogenic/abiogenic structure. In order to optically separate the two calcite phases forming a single calcite fibre, we employed a wide range of state-of-the-art analytical tools to thin sections and ultra-thin sections of well-preserved specimens. Pending a verification of these well-supported ultrastructural data by means of high-resolution geochemical analyses from biogenic and abiogenic phases, we suggest that these findings have significance for those using belemnite rostra as archives of their palaeoenvironment.

Cover Letter

Dr. René Hoffmann
Ruhr Universität Bochum
Department of Earth Sciences
Institute of Geology, Mineralogy, and Geophysics
Branch Paleontology
Universitätsstrasse 150, Building NA2/132
44801 Bochum
Germany
E-Mail: Rene.Hoffmann@rub.de

Bochum 2016-05-30

Dear Editor,

We greatly appreciate the input from two expert reviewers and have implemented the (minor) comments (see revision notes) in nearly all cases. Where we decided to not follow the reviewer's advice, we argue why we do so.

Thank you for your professional work!

Kind regards,

R. Hoffmann on behalf of the authors

Revision Notes

Dear Editor,

We greatly appreciate the input from two expert reviewers and have implemented the (minor) comments in nearly all cases. Where we decided to not follow the reviewer's advice, we argue why we do so.

General: We have included line numbering. Changed text passages are given in italics.

Reviewer SEDGEO5702_revDF – Reviewer 1

Comments made directly in the manuscript:

Line 94:

Belemnite rostra are traditionally considered to secrete their endoskeleton in oxygen isotope equilibrium with ambient seawater...

Belemnites are traditionally considered to secrete their endoskeleton in oxygen isotope equilibrium with ambient seawater...

Comment: We agree with the reviewer, not the belemnite rostra secrete their endoskeleton but the belemnite animal.

Line 127:

Thin sections (30 µm) and ultra thin sections (< 10 µm) of two well-preserved specimens of *Megateuthis gigantea...*

Thin sections (30 µm) and ultra thin sections (< 10 µm) of two well-preserved orthorostra of *Megateuthis gigantea...*

Comment: We agree with the reviewer that it is useful to distinguish between the orthorostrum and the epirostrum, both are present in *Megateuthis*.

Line 317-318:

Referring to the high porosity observed in both belemnite rostra and sepiid cuttlebone it is important to note that these structures are not homologous (Fuchs 2012).

Comment: We agree with the reviewer and added one sentence pointing out that the belemnite orthorostrum and the sepiid cuttlebone are not homologue structures. See below.

Line 334:

Apical region

Apical line region

Comment: We agree with the reviewer that it is better to refer to the apical line region connecting all apical regions during ontogeny instead of the apical region.

Line 359:

...outside of (i.e., the belemnite animal itself)...

... outside of the orthorostrum (i.e., the belemnite animal itself)...

Line 424:

shell

cuttlebone

Comment: To avoid further confusion between the belemnite rostrum and the tiny rostrum or apical spine at the posterior end of the sepiid cuttlebone, we used the general term cuttlebone for the latter which includes the highly porous phragmocone (see below).

Line 425:

...belemnite skeleton...

...belemnite orthorostrum...

Comment: As pointed out earlier by the reviewer it is more precise to refer to the orthorostrum instead of the whole belemnite skeleton which would include the phragmocone as well – which has a different mineralogy and ultrastructure and was not analysed in this study.

Line 428:

...living belemnites...

...living belemnite rostra

Comment: Changes accordingly to the comment by the reviewer.

Line 434:

...ommastrephid...

...*onychoteuthid*...

Comment: We changed the text accordingly to the comment by the reviewer.

Line 495:

Reviewer question: Does this concentration refers to the entire cuttlebone or only the sepiid spine ("rostrum")?

Comment: All cited references refer to the *Sepia* cuttlebone and do not specify a particular region, e.g., the spine.

Lines 518-521:

This tentative interpretation presented here with regard to belemnite rostra is arguably consistent with observations of 10-40% organic matrix in the *Sepia* cuttlebone (Birchall and Thomas, 1983; Florek et al., 2009). This is relevant as we suggest that the belemnite rostrum is structurally similar to the *Sepia* cuttlebone with regard to the primary intra-skeletal porosity.

This tentative interpretation presented here with regard to belemnite rostra is arguably consistent with observations of 10-40% organic matrix in the Sepia cuttlebone (Birchall and Thomas, 1983; Florek et al., 2009). This is relevant as we suggest that the belemnite rostrum is structurally similar but not homologous (Fuchs 2012) to the Sepia cuttlebone with regard to the primary intra-skeletal porosity.

Comment: The reviewer suggested to highlight here that the rostrum and sepiid cuttlebone are structurally similar, but not homologous. Accordingly, we added “but not homologous” to the text citing the work of Fuchs (2012). However, a discussion about the similarities and differences of the sepiid and belemnite rostrum is far beyond the scope of this paper.

Comments to the authors:

Reviewer #1: Dear authors, in some places, you compare the belemnite rostrum with sepiid cuttlebones. I recommend to provide a short explanation about the homologous shell parts of belemnites & sepiids. A clear differentiation between rostrum & phragmocone is essential to correctly interpret/comprehend observed porosities. In this context, it would be less confusing to compare the belemnite rostrum with the "rostrum" of sepiids and belosepiids (rather than their phragmocone).

Comment: We agree with the reviewer that the comparison of a belemnite rostrum with the Sepia cuttlebone might be misleading when it comes to the phylogenetic reconstruction of coleoid evolution. However, the reconstruction of coleoid phylogeny is far beyond the scope of our paper. Further, it should be noted that there is an open discussion about the homologous shell parts in fossil and modern coleoids and that authors cited in our manuscript did not distinguish between the different shell parts, e.g., Florek et al. 2009 reported on the amount of organic matter for the whole cuttlebone and did not distinguish between phragmocone, dorsal shield, and rostrum. In order to avoid additional confusion we decide to keep the comparison between the belemnite orthorostrum and the Sepia cuttlebone (which refers to the complete internal shell). We do so specifically because earlier authors, when describing porosity observed in belemnite rostra, compared it with the porous structure of the Sepia cuttlebone not distinguished between the phragmocone and other shell parts. For the "rostrum-problem" the reader is referred to Fuchs (2012). As far as we know no detailed description of the sepiid rostrum is available.

Apart from this, I would avoid the term "skeleton"; if then only in terms of the entire shell; not only shell parts, e.g. the rostrum.

We agree with the reviewer and delete whenever it seemed adequate the term skeleton.

I´m missing a paragraph discussing and verifying earlier observations/ ideas: who postulated a low porosity and what was wrong in the line argumentation?

We provide information about earlier observations of pore space or the varying amount of organic matter in belemnite orthorostra in the introduction part (lines 84-92) and in chapter 4.3 citing the most important articles by Müller-Stoll, Spaeth, and Saelen. Müller-Stoll (1936) argues for varying amounts of organic matter in the observed lighter/darker concentric rings, while Spaeth (1971, 1973, 1975) was the first who described a higher amount of porosity (up to 20%). In his extensive review Saelen (1989) comes to the conclusion that it is most likely that the belemnite rostrum was a dense structure already during life time of the belemnite animal. The latter statement (Saelen 1989) agrees with the majority of contemporaneous and all subsequent researchers (e.g., Veizer 1974, Podlaha et al. 1998) largely neglecting the porosity in belemnite rostra. Maybe this was due to the fact that Spaeth could only present data for a single belemnite rostrum (Neohibolites). To keep the focus on our description of the new ultrastructure and to avoid duplication we do not provide an additional paragraph discussing and verifying earlier observations dealing with the belemnite porosity.

Reviewer SEDGEO5702 Review 27 April 2016 IJ comments – Reviewer 2

All minor corrections were implemented in the revised version of the manuscript.

Line 275:

Reviewer question: Why specifically choose these elements for mapping? Common substitutions in the calcite lattice such as Sr, Ba, Fe, Mn, Zn are not mentioned. Do these not show any variation?

Comment: Fe, Mn content was quantitatively assessed using the cathodoluminescence microscope. Both show slight variation between the biogenic precipitates and secondary cement phases. We

specifically choose Mg, P, and S to collect arguments for the distribution of primary organic matter as we discussed in our manuscript.

Line 355:

... the dense fabrics observed in the case of most rostra collected in Mesozoic sedimentary successions...

... *the dense fabrics observed in rostra collected in Mesozoic sedimentary successions*...

Comment: We agree with the reviewer that it is surprising that no examples of preserved pore space exist as far as we know. However, fossil echinoderm remains, with a primary comparable porous endoskeleton, are also preserved as massive fossil structures with nearly no pore space left. Some belemnite rostra are preserved as hollow tubes thanks to strong diagenetic alteration processes. In some cases the outer margin of belemnite orthorostra show increasing porosity. This porosity is taken as sign of diagenetic alteration and does not resemble the described ultrastructure.

Line 384:

Reviewer statement: Yet echinoderm calcite commonly retains its intraparticle porosity in geological samples, despite being Mg-calcite!

Comment. We do not agree with the reviewers statement. Based on our own observations the majority of the primary pore space in echinoderm skeletons is occluded by secondary calcite (see also Dickson 2001, 2002, 2004). However, due to staining it is possible to reveal the original skeletal structure and distinguish it from the secondary cement phase.

Line 510:

Reviewer question: Are there any examples of cuttlebone being preserved in the way that you propose for belemnites?

Comment. As far as we know the ultrastructure of fossil sepiid cuttlebones is not described in comparable details. Further, no taphonomic framework for fossil cuttlebones is available.

Comments to the authors:

Reviewer #2: (1) The authors state (p14) that "The presence of a highly porous primary rostrum architecture during the life time of the belemnite organism as proposed here, is contrasted by the dense fabrics observed in the case of most rostra collected in Mesozoic sedimentary successions (Fig. 1A-B)."

They state "most", implying that not all belemnites have dense fabrics? I find it rather surprising that if their hypothesis is correct, why no examples of preserved porous calcite guards have ever been found. Is there any evidence of the existence of these, perhaps having been dismissed as 'altered' or 'leached' specimens? Such material would lend strong support to your hypothesis.

Comment. We agree with the reviewer that it is surprising that no examples of preserved pore space exist as far as we know. We have collected belemnite rostra from many different localities (Russia, Japan) while the primary intention was to collected hollow ammonites. Hollow ammonite preservation is very rare and requires special conditions. It can be assumed that belemnites collected from the same beds share a similar unique taphonomy. However, also those belemnite rostra collected together with hollow ammonites show a massive structure. Some belemnite rostra are preserved as hollow tubes thanks to strong diagenetic alteration processes. In some cases the outer margin of belemnite orthorostra show increasing porosity. This porosity is taken as a sign of diagenetic alteration and does not resemble the described ultrastructure. By the observation of darker and lighter concentric rings earlier researchers speculated about varying amounts of organic within these rings. Recently, Ullmann et al. (2015), based on geochemical analyses, postulated a 40% porosity for the apical line region. It was assumed by Ullmann et al. (2015) that the porosity decreases towards the rostral margin. Concluding, as far as we know no pore space had been described so far the fits with the herein described ultrastructure.

(2) The authors refer to the microstructure of echinoderm calcite (p16). They do not mention that echinoderm skeletons are also porous and subject to diagenetic infill. Yet echinoderm calcite may sometimes retain its intraparticle porosity even in Palaeozoic samples, despite originally being Mg-calcite! Why should belemnites be so uniform in their preservation style? A consequence of their unique crystallography?

Comment. We do not agree with the reviewers statement. Based on our own observations the majority of the primary pore space in echinoderm skeletons is occluded by secondary calcite (see also Dickson 2001, 2002, 2004). However, due to staining it is possible to reveal the original skeletal structure and distinguish it from the secondary cement phase.

(3) Cuttlebone is presented as the closest modern analogue to belemnite guards (e.g. p20). This seems to be perfectly logical. However, again, are there any examples recorded of cuttlebone being preserved in a similar manner to that proposed for belemnites? If the mechanism is valid, it seems rather surprising that no similar processes have been observed / described, even if only in a more superficial way. The different taphonomy a consequence of their aragonite mineralogy perhaps?

Comment. Sepiid cuttlebones are rather rare compared to the globally distributed and highly abundant belemnite rostra. We assume the different preservation originally lies in their different primary mineralogy (low Mg calcite for belemnites and aragonite for sepiids).

Thank you for your professional work!

Kind regards,

R. Hoffmann on behalf of the authors

Evidence for a composite organic-inorganic fabric of belemnite rostra: Implications for palaeoceanography and palaeoecology

Hoffmann, R.[1], Richter, D.K.[1], Neuser, R.D.[1], Jöns, N.[1], Linzmeier, B.J.[2], Lemanis, R.E.[1], Fusseis, F.[3], Xiao, X.[4] and Immenhauser A[1]

[1] Department of Earth Sciences, Institute of Geology, Mineralogy, and Geophysics; Ruhr-Universität Bochum, Universitätsstrasse 150, 44801 Bochum, Germany

Corresponding author. E-mail address: rene.hoffmann@rub.de (R. Hoffmann), phone number: +49-234-3227769

[2] Department of Geoscience, University of Wisconsin – Madison, 1215 West Dayton St, Madison, Wisconsin, USA

[3] School of Geosciences, The University of Edinburgh, Grant Institute, King's Buildings, West Mains Road, Edinburgh, UK EH9 3JW

[4] Advanced Photon Source, Argonne National Laboratory, 9700 S. Cass Ave., Lemont, IL, 60439 USA.

Formatted: Font: 14 pt, Bold
Formatted: Numbering: Continuous
Formatted: Font color: Auto

Abstract

Carbonate skeletons of fossil marine organisms are widely used to reconstruct palaeoceanographic parameters. Specifically, the geochemistry of Jurassic and Cretaceous belemnite rostra is traditionally interpreted to represent near sea-surface ~~palaeoenvironmental parameters~~seawater properties. More recently, an increasing number of workers, ~~however, report a~~have reported significant scatter in geochemical data (e.g., $\delta^{18}O$, $\delta^{13}C$, element/Ca ratio) when comparing rostra from the same stratigraphic level or within a single belemnite rostrum. This scatter is not explained by differential diagenetic overprint alone. Here we report petrographic evidence on the primary ultrastructure of rostra of *Megateuthis* (Middle Jurassic) and *Belemnitella* and *Gonioteuthis* (Late Cretaceous). The biogenic ultrastructure consists of a filigree framework of triaxial branches and tetrahedrons of variable size forming a honeycomb-like network. Data presented here suggest that these rostra yielded as much as 50 to 90% primary pore space. On the level of a working hypothesis - and in analogy with ~~Recent~~ modern cephalopods - we propose that the pore space was formerly filled with body fluid and/or organic compounds during the life time of these organisms. Intra-~~skeleton~~rostral porosity was post mortem occluded by earliest diagenetic isopachous calcite cements of a non-biogenic origin. These may have been precipitated due to increased alkalinity related to the decay of organic matter. If this holds true, then the resulting fabric represents a composite biogenic/abiogenic structure. In order to optically separate the two calcite phases forming a single calcite fibre, we employed a wide range of state-of-the-art analytical tools to thin sections and ultra-thin sections of well-preserved specimens. Pending a verification of these well-supported ultrastructural data by means of high-resolution geochemical analyses from biogenic and abiogenic phases, we suggest that these findings have significance for those using belemnite rostra as archives of their palaeoenvironment.

Keywords: belemnite, ultrastructure, carbonate archive, diagenesis, Jurassic-Cretaceous

1. Introduction

The ultrastructure of recent biogenic carbonates is of great interest for those concerned with biomineralization research in general (Weiner and Addadi, 2011; Goetz et al., 2011), those studying the primary biogenic skeletal structures of fossil skeletal hardparts (e.g., Coronado et al., 2013), and for palaeoceanographers exploring these materials for their bearing on past climate dynamics (Saelen, 1989; Cochran et al., 2003; Parkinson et al., 2005; Jarvis et al., 2015; Immenhauser et al., 2016). Whereas the tests of planktonic and benthic foraminifera (and coccoliths etc.) are important archives of open marine environments throughout the Cenozoic and beyond (e.g., Zachos et al., 2001), much of what is known about Cretaceous and Jurassic palaeoceanography has been deduced from the geochemical archive of the calcareous rostra of extinct cephalopods, specifically belemnites (Dutton et al., 2007). Reasons for the wide use of these archive materials include their abundance in the fossil record, the diagenetically stable low-Mg calcite mineralogy of rostra (Veizer, 1974; Saelen, 1989), and the broad palaeobiogeographic distribution of belemnites in the marine Boreal and Tethyan realms, (e.g., Urey Urey et al., 1951; Voigt et al., 2003; Wierzbowski, 2004; McArthur et al., 2007; Dutton, 2007; Price and Page, 2008; Wierzbowski and Joachimski, 2009; Price et al., 2009 2011; Li et al., 2012, 2013). As with all biogenic carbonates, however, these archives undergo post- mortem diagenetic alteration, representing a major obstacle in carbonate research (Swart, 2015).

Characteristic geochemical patterns and fabrics in biogenic carbonate hardparts have been used to test for example molluscks (e.g., Cochran et al., 2003, Sessa et al., 2015, Immenhauser et al., 2016), brachiopods (Parkinson et al., 2005), or foraminifera (e.g., Huber and Hodell, 1996; Kozdon et al., 2011) for evidence of diagenetic alteration. In the case of ammonites, the degree of preservation of nacre tablets provides evidence with regard to the preservation of these exoskeletons, to name one example (e.g., Cochran et al., 2010). With regard to belemnite rostra, the observation of well-preservedan intact fibrous microfabrics in thin sections and polished rock surfaces in combination with cathodoluminescence is commonly used to identify well- preserved belemnite rostra (Rosales et

al., 2001). In contrast, cloudy areas, exfoliation, fractures, stylolites, or boring traces are interpreted as evidence for post -mortem alteration (Saelen, 1989; Li, 2011; Benito and Reolid, 2012). A rigorous discussion of screening techniques, including trace-element concentrations, and isotopic ratios applied to biogenic low-Mg calcite macrofossils, ~~is~~has been provided by Ullmann and Korte (2015). Similarly, a "best practice" approach for the interpretation of mollusc and brachiopod carbonate archives was presented ~~in~~ by Immenhauser et al. (2016).

The ultrastructure of belemnite rostra was first studied by Müller-Stoll (1936). This author described organic-rich (laminae obscura) and carbonate-rich (laminae pellucidae) concentric growth rings. Both of these were later shown to be calcitic but differ due to variable ~~degrees of~~amounts of occluded organic matter (Saelen, 1989). Growth rings are made up by fibrous calcite crystals radiating from a central zone called apical line (Richter et al., 2011) forming what seems to be a low-porosity fabric (Saelen, 1989 and references therein; Fig. 1A-C). Single fibres (= radial structures of Saelen, 1989) can be arranged in bundles traversing the concentric growth layers. Each fibre thickens outwards and shows a sub-fibrous framework potentially first proposed - but not further explored - by Saelen (1989, Fig. 15a).

Belemnites ~~rostra~~ are traditionally considered to secrete their endoskeleton in oxygen isotope equilibrium with ambient seawater (e.g., Anderson et al., 1994; Price and Sellwood, 1997; Voigt et al., 2003; Price et al., 2009; Wierzbowski and Joachimski, 2007, 2009). The main argument brought forward is commonly the presence of what are considered cyclical oxygen isotope patterns interpreted as seasonal seawater temperature variations (Urey et al., 1951). The PeeDee belemnite used in Urey´s study was considered as well-preserved based on the compact fabric and the optical features of the calcite crystals (but see Li, 2011 for discussion). The assumption of equilibrium precipitation was further supported by data sets from recent cephalopods including *Nautilus*, *Sepia*, and *Spirula* precipitating their skeletal hardparts in near-equilibrium with $\delta^{18}O_{seawater}$ (Lukeneder et al., 2010). In contrast to this traditional view, there is an increasing amount of evidence suggesting that belemnite rostra are problematic archives of their palaeoenvironment (see Immenhauser et al.,

2016 for detailed discussion). For example, Price et al. (2015) reported an offset of about 5°C between the aragonitic phragmocone and the calcitic rostrum of a single specimen of *Cylindroteuthis*. This offset was regarded as vital effect but it remains unclear whether the temperatures derived from the aragonite are too warm or from the calcite too cool. Similarly, high intra-rostral variability of elemental (Ca, Mn, Mg, Fe, Sr) and isotopic ($\delta^{18}O$, $\delta^{13}C$) composition, the latter with a scatter of up to 2‰, has been reported from belemnite rostra lacking evidence for diagenetic alteration (Podlaha et al., 1998).

The significant discrepancy of these data sets forms a strong motivation for a reconsideration of belemnite rostra as archives of their palaeoeonvironment. Here, we report data from a wide set of state-of-the-art analytical infrastructure applied to thin- and ultra-thin sections of exceptionally well-preserved Jurassic and Cretaceous belemnite rostra. The following aims guided this paper: First, to present well-constrained petrographic evidence for the complex primary biogenic framework of these rostra; second, to document evidence that points to athe highly porous nature of this biogenic framework; third, to assess the relative proportion between primary skeleton and porosity; fourth, to discuss the timing and nature of the pore-filling calcites phase. Evidence reported here has significance for the interpretation of proxy data from ancient belemnite rostra and forms the foundation of a detailed, high-resolution geochemical study that will be in the focus of forthcoming work.

2. Materials and Methods

2.1. Belemnites

Thin sections (30 µm) and ultra- thin sections (< 10 µm) of two well-preserved ~~specimens~~ orthorostra of *Megateuthis gigantea* (Schlotheim, 1820) from the Middle Jurassic~~)~~ and one specimen of *Belemnitella mucronata* (Schlotheim, 1813) and *Gonioteuthis quadrata* (Blainville, 1827) from the Upper Cretaceous~~)~~ were studied. Specimens of *Megateuthis* were collected in Bajocian marly

limestone deposits from southern Germany. *Belemnitella* rostra are from the late early Campanian (*mucronata* Z~~z~~one), and *Gonioteuthis* from the early Campanian *lingua*/*quadrata* – *gracilis*/*mucronata* Z~~z~~one from northwestern Germany. *Gonioteuthis* and *Belemnitella* rostra were embedded in calcareous (65-90%) epicontinental shelf deposits of the Misburg ~~f~~Formation (Niebuhr, 1995; Niebuhr et al., 2007). Specimens did not display evidence for exfoliation nor did they show boring traces of the surfaces of rostra. Specimens were sectioned along their long axis in a marginal position and perpendicular to the c-axis of their calcite fibres. One section cuts the rostrum of *Megateuthis* perpendicular to the long axis.

Formatted: Font: Italic, No underline, Font color: Auto

Formatted: Font: Italic, No underline, Font color: Auto

Formatted: Font: Italic, No underline, Font color: Auto

Formatted: Font: Italic, No underline, Font color: Auto

Formatted: Font: Italic, No underline, Font color: Auto

2.2. Methods

Surfaces of thin sections were chemo-mechanically etched using colloidal silica (OP-S) for 5-15 minutes to reduce surface irregularities on an atomic scale (Massonne and Neuser, 2005) and coated by a thin carbon layer. All coated thin sections have been studied under a high-resolution field emission scanning electron microscope (HR-FESEM) type LEO/ZEISS 1530 Gemini using a backscatter detector (BSD) at the Ruhr-Universität Bochum, Germany (Figs. 1-3).

Crystallographic orientation of belemnite calcite fibres was determined by electron backscattered diffraction (EBSD; Nordlys, OXFORD Instruments). The data acquisition and analysis was performed using the software packages AZtec and Channel 5 by Oxford Instruments (Fig. 4). The scanning electron microscope (SEM) was operated at beam energy of 20 kV, an aperture of 60 µm, a working distance of 25 mm and a tilt angle of 70°. Thin sections were mapped at Bochum University in the high-resolution mode using a grid matrix (1149x748 points) at a step ~~rate~~ width of 2.017 µm (Fig. 4A) and (543x266 points) at a step ~~rate~~ width of 1.652 µm (Fig. 4D) and for the single calcite fibre 50 µm to reduce artefacts and increase the reliability of the data. The orientations of the crystals ~~of~~ in the individual maps were visualized using a rainbow colour coding ranging from blue over green and yellow to orange and red, where identical colours indicate identical crystal axis

orientations. For visualizing the weak angular deviations in the crystal lattice in a single calcite fibre, we applied an angular resolution of 2 degrees for the complete rainbow colour range. In addition, orientations of the measured crystallographic axes ~~a~~were plotted into the lower hemisphere of a Schmidt net (Fig. 4E).

Rostra were further investigated under a cathodoluminescence microscope type HC1-LM by Lumic equipped with a hot cathode (Neuser et al., 1996) and a digital camera system (DP73 by Olympus) for recording digital images at Bochum. Beam energy of 14kV and a beam current density between 5 and 10 µA/mm² were generally used for the CL-measurements. Integration times for CL-spectra were commonly between 10 and 60 seconds (Fig. 5).

X-ray element distribution maps were acquired using a Cameca SX5FE field emission electron microprobe at Bochum. The acceleration voltage was 15 keV with a probe current of about 80 nA and a fully focused beam. The intensity of S Kα1 was recorded simultaneously on two wavelength dispersive spectrometers equipped with LPET and PET analyzing crystals. The Mg Kα1 line was also measured on two spectrometers (LTAP and TAP crystals), whereas P Kα1 was measured on a single spectrometer equipped with a LPET crystal. The images were acquired in continuous stage scan mode. They have a resolution of 2048 x 1536 pixel, and the dwell time was 17 ms per pixel (Fig. 6).

To test for the distribution of organic matter within the belemnite rostra, thin sections were studied under ~~the~~a fluorescence microscope (Leica DM4500P) equipped with a mercury short-arc reflector lamp coupled with a Leica EL6000 compact light source. We used the blue light filter set producing bright green fluorescence images (filter set I3 for blue light excitation: excitation 450-490 nm, emission 515 nm, voltage 100-240 VAC and 50-60 Hz frequency; Fig. 7). Fluorescence microscopy in the manner applied here is an optical tool to qualitatively document the spatial distribution of organic matter in shells. Fluorescence reflects organic matter and less commonly crystal lattice defects and solid inclusions in crystals. Fu~~o~~rther ~~more~~ details of this method~~s~~ have been presented ~~please refer to~~by Wanamaker et al. (2009) and Ritter et al. (subm.).

Confocal laser fluorescence microscopy (CLFM) images on an uncoated *Megateuthis* mount were made using a Bio-Rad MRC-1024 scanning confocal microscope at the W. M. Keck Laboratory for Biological Imaging at UW-Madison (Fig. 8). The microscope was operated with a 40 mW laser at wavelengths of 488 nm, 568 nm, and 647 nm. All three wavelengths were simultaneously rastered across the sample. Naturally occurring compounds within the sample caused fluorescence at multiple wavelengths. Images were collected through the following three emission filters: visible green light (λ = 505 to 539 nm), visible red light (λ = 589 to 621 nm), and far-red light (λ = 664 to 696 nm).

In order to analyze the three dimensional filigree framework, synchrotron radiation based micro-computed tomography was applied (Fig. 9). Data were collected at the bending magnet beam line 2-BM at the Advanced Photon Source, Argonne National Laboratory, USA. A double multilayer monochromator of 1.5% band-width provided 27.2 KeV X-rays. Images were collected in transmission mode by a CCD camera behind the sample in the hutch configuration. The sample-detector distance was set to 300 mm to collect quantitative phase contrast data. 1440 projections were acquired while the sample was rotated over 180° in steps of 0.125°. A microtomographic data set with a size of 2048 x 2048 x 1948 voxels was reconstructed using a phase retrieval algorithm (Mokso et al., 2013).

3. Results

3.1 Optical-, cathodoluminescence-, fluorescence-, and confocal laser fluorescence microscopy (TL, CL, FL, CFLM)

Under transmitted light (TL), thin sections of rostra cut perpendicular to the c-axis of calcite fibres reveal a banded distribution of calcite fibres containing brownish triangular elements of variable size (Fig. 5A, D). Some of the larger fibres contain a triangular, organic-rich centre, with its innermost domains occluded by translucent calcite. Bundling of neighbouring calcite fibres is indicated by their subparallel orientation of their a-axis (Fig. 5D). A uniform extinction (orientation)

pattern of adjacent fibres under crossed polarizers is observed (Fig. 5B, E) and is in agreement with EBSD data (Fig. 4A). Individual fibres display an undulatory extinction (converging or diverging c-axes) under crossed polarizers. Calcite occluding space between organic-rich elements and fibre reinforcement is translucent and contains little or no organic matter (Fig. 5D). Brownish, triangular elements have a relatively low optical relief, compared to the surrounding translucent calcite with a relatively higher optical relief (supplement Fig. 1A-B).

Three different luminescence patterns are observed under the cathodoluminescence microscope (CL): (i) A light blue luminescence of the brownish, triangular elements (Fig. 5C, F); (ii) dark blue, intrinsic luminescence of the translucent phase; (iii) locally, orange to red luminescent fractures and microstylolites are observed. In rare cases, fractures retrace the triangular outline of a fibre (Fig. 5C, F, supplement figure 1D).

Brownish triangular areas under transmitted light display light green fluorescence while the translucent areas show a dark green fluorescence under the fluorescence microscope (FL). Microfractures are darker under transmitted light compared to the triangular elements and show a light green fluorescence (Fig. 7A-B).

Different fluorescence patterns under the CLFM reveals calcite domains visible in BSE (and other) imaging techniques (Figs. 3, 5-7). Filled cracks fluoresce brightly in green and red wavelengths (Fig. 8B-C). Domains that are dark in BSE do not fluoresce in CLFM (Fig. 8A-D). Bright domains in BSE fluoresce brightly in CLFM at all wavelengths observed (Fig. 8A-D). Higher magnification reveals brighter fluorescence between adjacent domains that appear bright in BSE (Fig. 8D).

3.2 Scanning-electron microscopy equipped with a backscatter detector (SEM BSD)

Images collected with the scanning electron microscope equipped with a backscatter detector present important evidence for the presence of two calcite phases (dark and bright) of different

chemical compositions building the rostra studied. The brownish triangular areas under transmitted light are dark in BSE. Thin sections cut perpendicular to the c-axis of the radiaxal fibrous calcite (Fig. 1D I-IV) reveal a complex framework, dark in BSE, surrounded by relatively brighter calcite (Figs. 1-3). Cross sections of the majority of fibres are polygonal or, less often, honeycomb shaped with a tri-radial (120°) symmetry representing an ultrastructure that has not ~~yet~~ been described in previous studies (Figs. 1C-G, ~~Fig.~~ 3A-E). Individual fibre diameters vary between 10-80 µm. Calcite fibres terminate at individual concentric growth layers that also form the nucleation site for the overlying, next fibre generation, displaying increasing thicknesses and occurring in increasing numbers towards the outer portions of the rostrum (Fig. 1A-D). Brighter area in BSE are more likely to be composed of near-stoichiometric $CaCO_3$ with higher average atomic masses (mainly Ca), whereas excess C, P, Mg, or S will lower the average atomic mass. Accordingly, areas with decreasing amount of Ca and increasing amounts of C, P, Mg or S are darker.

Four section planes are presented to describe the intricate bio-composite mineral present within a single fibre. The following description distinguishes between the darker framework (i), i.e., micro~~n~~metre-thick branches terminating in wall-like reinforcements and (ii) tri-radial central portions; and brighter fabric (iii) consisting of calcite crystals forming isopachous cement layers with individual crystallites coated by submicro~~n~~metre thick layers of matter darker in BSE (Fig. 1G). In all sections, we observed isopachous calcite crystals oriented perpendicular to the inner dark walls (Fig. 3A-E). Section plane I consists of three simple, dark in BSE branches of variable lengths. Often, these branches exhibit reinforcements of variable lengths and thicknesses (about 1 micro~~n~~metre) and increasing widths towards neighbouring branches (Figs. 1D-I, 3A). Conversely, reinforcements being connected to neighboring triangles are rarely observed. Section type II is characterized by an enlarged, dark in BSE central element of variable diameter (2-30 µm, Figs. 1D-II, 3C). Some of the larger central elements display an inner zone with additional tri-radial structures comprising of smaller, isopachous, brighter in BSE area calcite crystals rotated by 60° relative to outer branches (Figs. 1D-III, 3D; section type III). Section type IV represents the most complex fabric. Here, the inner

portions of larger central elements display alternating darker and brighter in BSE areas (Figs. 1D-IV, 3E). Generally, enlarged central elements correlate with a shortening of corresponding, darker branches.

Thin sections cut parallel to the c-axis of the radiaxial fibrous calcite reveal an framework dark in BSE of triangular shaped elements with their tips pointing towards the outer margin of the rostrum (Fig. 1C-D, supplement Fig. 2). Lighter and darker areas within a single calcite fibre show their composite nature. Lighter and darker areas within concentric growth rings, as visible in transmitted light, depend on the number and size of these elements. Higher magnification reveals a homogenous central portion ("trunk" – white line) of pyramidal morphology dark in BSE surrounded by inclined isopachous calcite crystals coated by material dark in BSE. This overall pattern results in a "~~x-~~ Christmas tree like" structure (Fig. 3F). The dark framework forms the substratum upon which an isopachous, translucent calcite phase nucleated (Fig. 1D, G 2-3). The boundary surface between the framework dark in BSE and the surrounding carbonates brighter in BSE is, in places, corroded and uneven (Fig. 2).

3.3 Electron microprobe analysis (EMPA)

The contrasting chemical composition of the two different calcite phases building these rostra is also revealed by EMP data. Detailed WDS scans show that the strongest variability is displayed by Mg, P, and S, whereas other elements are almost constant or ~~contained~~present in amounts close to the detection limit (e.g., SrO = 0.1-0.2 wt.%; FeO = <0.1 wt.%; MnO < 0.5 wt.%. X-ray element distribution ~~counts~~ maps show a generally low concentration of the elements Mg (MgO = 0.3-0.4 wt.%), P (P_2O_5 = 0.1-0.2 wt.%), and S (SO_3 = 0.20-0.50 wt.%). The Mg- and P-content is slightly elevated in the darker, triangular areas in BSE images (MgO up to 0.6 wt.%; P_2O_5 up to 0.25 wt.%) compared to the relatively brighter areas in BSE images in the centre of larger tetrahedrons and their ~~surroundings~~vicinity. Lowest Mg ~~values~~ concentrations were ~~collected~~ found along microfractures

Formatted: No underline, Font color: Auto

Formatted: Font: +Body, No underline, Font color: Auto

Formatted: Font: +Body, No underline, Font color: Auto

Formatted: Font: +Body, No underline, Font color: Auto

Formatted: No underline, Font color: Auto

Formatted: No underline, Font color: Auto

Formatted: No underline, Font color: Auto

Formatted: No underline, Font color: Auto

that ~~show a~~display bright luminescence ~~in CL~~colours (MgO < 0.2 wt.%; Fig. 6B). Sulfur has a higher concentration in the brighter ~~in BSE~~ areas in BSE images (SO_3 up to 0.65 wt.%) and lower concentrations in the darker areas in BSE ~~area~~images (~~:~~SO_3 = 0.20-0.50 wt.%; Fig. 6D). For better comparison with BSE images from other samples and with the element distribution, ~~we collect~~ BSE data were obtained for the same field of view (Fig. 6A).

3.4 Electron Backscattered Diffraction imaging (EBSD)

Electron backscattered diffraction was used to document the biological controlled (sensu Lowenstam and Weiner, 1989; Dupraz et al., 2009; Weiner and Addadi, 2011) formation of what is here assumed to represent the primary biogenic skeletal carbonate. EBSD reveals a very low variation of c-axes orientation of calcite fibres (Fig. 4A). The sub-parallel orientation of the c-axes {001} is documented by their close fitting in the lower hemisphere of a Schmidt net (Fig. 4E, left plot). A different characteristic is found for the crystallographic orientation of the a-axes {010} of calcite fibres (Fig. 4E, right plot). All a-axes are aligned along a great circle whilst the colour code of the according fibres is indicative of an arrangement in bundles. Adjacent fibres (10 to 100 fibres) share a similar - if not identical - orientation (Fig. 4A-B). The majority of fibre bundles are characterized by blue, green and red colour coding. Specifically, the spatial orientation of individual a-axes within a single fibre bundle deviates by 20° or less from the bundle mean value. Variation in the orientation of the c-axis of a single calcite fibre in the range of 1-3° was observed (Fig. 4D). As the angular resolution from blue to red rainbow colour shown in EBSD maps (Fig. 4A-B) has a resolution of 50°, minor angular deviations (<1°) are not visible in ~~our image~~ Fig. 4A-B.

3.5 *Synchrotron radiation based micro-computed tomography (SRμCT)*

Formatted: No underline, Font color: Auto

Formatted: No underline, Font color: Auto

Formatted: Font: +Body, No underline, Font color: Auto

Formatted: No underline, Font color: Auto

Formatted: Font: +Body, No underline, Font color: Auto

Formatted: No underline, Font color: Auto

Formatted: Font: +Body, No underline, Font color: Auto

Formatted: No underline, Font color: Auto

Tetrahedral structures are visible in three dimensions in the tomographic dataset despite the high signal to noise ratio and artefacts. There is a distinct difference in X-ray attenuation between the inner tri-radial elements and the surrounding calcite.

4. Interpretation and Discussion

4.1 Reconstruction of the primary belemnite rostrum ultrastructure

Data presented here document a repeated pattern of triangular elements that seem to be originally connected, building a concentric layered, highly complex, and porous framework. The space between the former skeletal elements is interpreted as pore space probably filled by body fluids or organic material during the life time of these organisms. The latter assumption is based on analogous observations in the porous endoskeletons of recent *Sepia* (Sherrard, 2000; Guerra, 2006). Referring to the high porosity observed in both, the belemnite rostraum and the sepiid cuttlebone, it is important to note that these structures are not homologous (Fuchs 2012).

Accordingly, the belemnite rostra originally consisted of an organic-rich biogenic framework of calcitic tri-radial tetrahedrons (triangular pyramids arranged perpendicular to the concentric layers during lifetime). Tetrahedrons are elongated along their c-axis with the tip of the pyramid pointing towards the precipitation site i.e., in growth direction towards the outer margin of the rostrum (Fig. 1C-D). Individual branches protruding from the edges of the tetrahedrons possess outer reinforcements acting as stabilizers. The central portion of the tetrahedrons may yield a channel-like cavity (Fig. 1D III-IV). Organic membranes at which nucleation of the tetrahedrons may have started and stopped are not preserved. However, it seems likely that such membranes were present because the bases of the tetrahedrons follow a concentric layer. Structurally, the bundling of the tri-radial elements forms a simple honeycomb-like framework in which the terminations of branches of

329 adjacent elements are connected. The mechanical stability of the honeycomb structure is enhanced
330 by reinforcement walls (Figs. 1D, G, 3C).

331 Based on the variable dimensions of skeletal elements seen in thin sections, intra-rostral pore
332 space was visually estimated to range between 50-90% of the total rostrum (Fig. 3A: 90% pore space
333 and 10% skeletal elements; Fig. 3B; 50% pore space and 50% skeletal elements). In this context, the
334 observation that pore space is not limited to the apical line region but is present across the bulk
335 rostrum is important. The secretion of a porous, but mechanically stable ~~endoskeleton~~ orthorostrum
336 is probably best seen in the context of a considerable reduction of energy and building material
337 required to form this structure compared to a massive ~~structure~~ endoskeleton (Sherrard, 2000).
338 Strict biological control, i.e. in the presence of organic templates (Chateigner et al., 2000; Richter et
339 al., 2011), over the precipitation of primary skeletal elements is demonstrated by a systematic
340 arrangement of adjacent elements into bundles of similar or identical orientation of their
341 crystallographic a-axes. This configuration results in a much higher mechanical load capacity and
342 torsion stiffness of the framework of the rostrum.

343 Alternating concentric Ca-rich (brighter; laminae obscurae) and C-rich layers (darker; laminae
344 pellucidae) of Müller-Stoll (1936) are related with the banded distribution of larger and smaller
345 organic-rich triangular elements of the primary skelet~~on~~al structure of the belemnite orthorostrum
346 (Fig. 1D, supplement Fig. 2). These layers potentially indicate differences in calcite precipitation rates.
347 Based on petrographic and ultrastructural evidence, the Mg and Ca elemental concentrations of the
348 rostrum, the lack of secondary micro-dolomite, and the absence of blotchy luminescence, the widely
349 held assumption of a primary low-Mg calcite mineralogy for the studied belemnite rostra is
350 confirmed (see discussion in Richter et al., 2003).

351

352 *4.2 Early and late diagenetic processes*

353

354 The presence of a highly porous primary rostrum architecture during the life time of the
355 belemnite organism as proposed here, is in contrast~~ed by~~to the dense fabrics observed in ~~the case of~~
356 ~~most~~ rostra collected in Mesozoic sedimentary successions (Fig. 1A-B). Hence, the diagenetic
357 pathway from porous to dense fabrics deserves attention. The marine diagenetic alteration of
358 biominerals is initiated directly after the death of a carbonate-secreting marine organism when
359 metabolic processes come to a halt. At this early stage, organic matter outside of the orthorostrum
360 (i.e., the belemnite animal itself) and in the pore space of rostra and between biominerals
361 decomposes (Saelen, 1989), triggering a series of complex bio-chemical processes. Essentially,
362 decomposition of organic matter is mediated by microbial activity, and given the abundance of
363 marine microbial life, there is no reason to assume that this would have been different in the case
364 examples studied here.
365 Microbial metabolic products, the presence of microbial "mucus" (extracellular polymeric
366 substance) and charged surfaces represented by microbial bodies influence the micro-environment
367 in intra-rostrum pore space by altering the balance between more reduced and more oxidized forms
368 of carbon as previously summarized under the term "alkalinity engine" (Dupraz et al., 2009).
369 Specifically, Visscher and Stolz (2005) subdivided microbial species into 5-7 groups ("guilds") having a
370 similar metabolism. Some of these promote carbonate precipitation (e.g., cyanobacteria, sulphate
371 reducers), whilst others favour dissolution (e.g., aerobic heterotrophs, fermenters). Dupraz et al.
372 (2009) documented that the balance of microbial metabolic activities directly influences carbonate
373 precipitation or, vice versa, dissolution. Initial microbial decomposition of organic matter may result
374 in the production of organic acids lowering the pH-values in the pore space (Berner et al., 1978),
375 enhancing intra-~~skeleton~~ orthorostrum dissolution of biominerals (Fig. 2).
376 As soon as the bulk of organic matter is decomposed, alkalinity is increased due to microbial
377 metabolic products enhancing the precipitation of carbonate minerals (intrinsic
378 organomineralization) leading – in the view of the authors - to the formation of the translucent,
379 isopachous calcite crystals that occlude primary pore space in rostra (Fig. 2). Obviously, any

assumption regarding microbial processes in these ancient carbonates must remain speculative. Nevertheless, following the basic concepts laid out in Dupraz et al. (2009), we tentatively assume that a first phase of decomposition was dominated by aerobic heterotrophy, sulphide oxidation, and fermentation decreasing the saturation index and resulting in the corrosion of skeletal elements in the belemnite rostrum. Evidence for this comes from micro-corrosion features at the outer surfaces of the primary skeletal framework forming the substratum upon which the pore-filling, secondary calcite phase nucleates (Fig. 2).

The nucleation and precipitation of the secondary calcite phase (Fig. 1D, G, 2-3) was possibly dominated by sulphate reduction increasing the saturation index and hence favoring precipitation of $CaCO_3$. During crystals growth, remnants of belemnite organic matter combined with microbial mucus were likely trapped between single crystals or at the growth front of crystals and delineate crystal boundaries. Specifically, the growth of fibrous calcitic crystals will proceed as long as growth rate, fluid supersaturation, and temperature are low enough to discourage spontaneous nucleation (Oti et al., 1989). Similar processes have been described from extant echinoderm endoskeletons ~~skeletal remains~~that share a comparable amount of primary porosity ~~like the herein~~with the described belemnite orthorostra (Richter et al., 2003).

During this early stage of diagenetic evolution, the rostra most likely preserved their original morphology due to the biogenic calcite framework and abiogenic calcite progressively occluding former pore space preventing, in combination, a collapse of the ~~endoskeletons~~rostra. The directly comparable, dark blue intrinsic luminescence of the translucent secondary outer calcite layer and the calcite infill of central pore space of many of the larger triangles (Figs. 3D-E, 5A, D, 6) suggest that both phases precipitated from one fluid, or different fluids with near-identical geochemistry. This is, of course, within the limitations of the geochemical resolution of the ~~CL~~ cathodoluminescence method and with reference to elements that affect luminescence patterns (e.g., Mn^{2+}, Fe^{2+} and REE; see discussion in Barbin 1991, 1993; Ritter et al., 2015). Conversely, the organic matter-rich triangles display a moderately brighter blue luminescence pattern (Fig. 5C, F). This feature is best explained by

calcite lattice deformation due to the incorporation of organic matter into the crystal lattice (intracrystalline) and is not necessarily indicative of a different geochemical composition. This concept is supported by x-ray diffractometry (Richter et al., 2011) documenting that the fibrous fabric of the belemnite rostra, lacking late diagenetic Mn-rich cements, is composed of stoichiometric or near-stoichiometric calcites (d (104) = 3.030 to 3.035 Å).

A late diagenetic (burial) stage of rostra is documented by dissolution and compaction features as indicated by microfractures and microstylolites (Figs. 2, 5C, F; Rosales et al., 2004a~~/~~, b). The circulation of Mn^{2+}-rich fluids caused the precipitation of a late calcite phase that occludes fractures and fissures. In some cases this late phase yields a bright luminescence and is zigzag or triangular shaped, tracing the morphology of the triangular biominerals (Fig. 5C).

4.3 Implications for the function of the rostrum

It is generally accepted that the belemnite rostrum acts as a counterweight to the soft body. Based on the observation of a high primary porosity (see also Spaeth, 1971, 1973, 1975; Ullmann et al., 2015), this interpretation requires renewed consideration. Rostra are commonly considered to have the same density as inorganic calcite crystals, ranging from 2.5-2.7 g/cm³.

Sepia, the closest living relative of the extinct belemnites, incorporates a total of 10-40% organic matter in its cuttlebone ~~shell~~ and comparably high amounts of intracrystalline organics were observed for the biogenic belemnite ~~skeleton~~orthorostrum. Accordingly, ignoring open pore space, a reduced density of the biogenic belemnite calcite of about 2.4 g/cm³ (10% organic) – 2.0 g/cm³ (40% organic) results. Assuming that liquid or extracrystalline organic matter (1.03 g/cm³) - with density comparable to that of seawater (1.026 g/cm³) - filled up the pore space of living belemnite rostra, an overall density of the rostrum ranging between roughly 1.7-1.1 g/cm³ (mean 1.4 g/cm³) is tentatively assumed on the level of a working hypothesis. If these assumptions hold true, then the belemnite

rostrum had a cumulative density that is significantly lower than that of stoichiometric calcite. Therefore, questions regarding the locomotion of belemnites result.

A possible analogue may come from a structure reported from a modern onychoteut~~mmastrep~~hid squid (*Onykia*) that has remarkable morphological similarity to the *Megateuthis* rostrum. *Onykia* has a purely organic rostrum that due to its very low density does not act as a counterweight for the soft body. It is assumed that it supports the posterior part of the mantle and fins (= axial stability in Bizikov and Arkhipkin, 1997 and Arkhipkin et al., 2015). A function as a muscle attachment structure for belemnite rostra ~~h~~was ~~been~~ first put forward by Stevens (1965). Direct evidence for the presence of fins in belemnites has recently reported by Klug et al. (2015), favouring a squid-like high speed swimming ~~in~~mode of life for Jurassic belemnites. Noteworthy to report here, is the case of belemnites (*Chitinoteuthis*) with a non-calcified rostrum (Müller-Stoll, 1936).

5 Open questions and suggestions for future research

5.1. Paragenesis of porosity-occluding calcite phase

Within individual belemnite rostra, data presented here differentiate: (i) a~~the~~ biogenic, highly porous skeletal framework secreted during the life time of the ~~belemnite~~organism; (ii) ~~the~~ an inorganic or organomineralic – arguably early diagenetic - calcite phase occluding the pore space of the biogenic framework; and (iii) a late diagenetic, burial, Mn-rich carbonate phase filling fissures and larger cracks within the rostra. Assuming that the above-discussed paragenetic succession is valid, a series of open questions result. ~~:~~ In the view of the authors, it is at least conceivable that portions of the rostral pore space were occluded during the life time of the belemnites (remote biomineralization sensu Hücker and Hemleben, 1976; Chinzei and Seilacher, 1993; Seilacher and Chinzei, 1993). If this holds true, then the paragenetic sequence of primary framework and secondary infill calcite is even more complicated than presented here and gradual in nature. Moreover, individual growth increments within rostra are then not representative of specific

457 correlative time intervals. Specifically, each growth increment then represents a complex composite
458 structure of paragenetic phases representing temporally different stages in the belemnite
459 ontogenetic cycle. Obviously, this would render the interpretation of time series belemnite
460 geochemical data difficult. Evidence against a biogenic infill of the skeletal pore space by remote
461 biomineralization sensu Seilacher and Chinzei (1993), however, may or may not come from the
462 presence of a corroded outer surface of what is considered the primary skeletal ultrastructure of
463 these rostra (Fig. 2). It seems difficult to argue that intra-rostrum body fluids became corrosive at
464 some stage during the life time of the belemnite animal. Clearly, these questions require further
465 detailed work.

466

467 *5.2 Primary skeletal ultrastructure and preservation of organic matter*

468

469 The authors acknowledge the fact that despite the very detailed information regarding the
470 belemnite ultrastructure shown here, our study lacks direct evidence for a primary biogenic origin of
471 the complex, highly porous framework and the subsequent cementation by an early diagenetic
472 calcite phase. Open questions, however, remain. Specifically, the significance of preserved organic
473 matter in the biogenic belemnite calcite deserves attention. In the following, we present several lines
474 (petrographic, optical, and geochemical data) of circumstantial evidence suggesting the presence of
475 preserved organic matter.

476 The sector-wise systematic arrangement of triangular elements - with their a-axis being
477 oriented subparallel to parallel (Figs. 3A-C, 4A-B, 5A, D) - in bundles, indicate a biologically controlled
478 origin (Lowenstam and Weiner, 1989) of these fabrics. The primary belemnite rostrum ultrastructure
479 is brownish (Figs. 5A, 7A) in thin sections under transmitted light and has a relatively low optical
480 relief. According to Ullmann et al. (2014), brownish areas in thin sections of biogenic carbonates are
481 indicative of remnant organic matter (C_{org}). Under the cathodoluminescence- and fluorescence
482 microscope, the primary filigree belemnite framework shows a light blue luminescence (CL) and light

green fluorescence (FL). According to Wanamaker et al. (2009) and Pérez-Huerta et al. (2008), fluorescence in biominerals is triggered by organic macromolecules associated with chitin polysaccharides and proteins. Dark fluorescence patterns commonly refer to portions of the skeletal hardparts that are relatively depleted in organic matter. Bright green fluorescence patterns typify areas with increased amount of organic matter (Wanamaker et al., 2009).

Primary skeletal structures display darker colours in SEM-BSE images. Electron microprobe analyses revealed that the biogenic skeletal calcites contain more P and Mg but less S compared to what is here considered an early diagenetic, pore-filling calcite phase. Higher concentrations of P (Fig. 6C) may be related to the presence of organic matter. Arguments for this have been presented by Longinelli et al. (2002, 2003) and Gröcke et al. (2003) who found phosphate (PO_4^{3-}) of presumed biogenic origin being preferentially enriched along concentric growth rings. Generally, the phosphate concentration of ancient belemnite rostra is variable but very low (less than 0.3%) comparable to that in ~~Recent~~ modern *Sepia*.

The primary filigree belemnite framework does not fluoresce under the CLFM. The factors that cause fluorescence in samples studied under the CLFM are poorly constrained (Fig. 8). Naturally-occurring organic compounds such as proteins or polysaccharides can cause fluorescence in other biogenic carbonates, including brachiopods (Pérez-Huerta et al., 2008), gastropods (Guzman et al., 2007), or cephalopods (Linzmeier et al., 2016). In modern brachiopods and *Nautilus*, portions of the exoskeletons with higher amounts of intracrystalline organic matter (Clark, 1999) appear dark under CLFM (~~-~~Pérez-Huerta et al., 2008; Linzmeier et al., 2016~~; Pérez-Huerta et al., 2008~~). This pattern lends support to the argument that dark triangular areas in BSE images represent the primary biogenic skeleton and contain remnants of organic matter. Marine sediments may contain abundant humic substances resulting from the degradation of marine organic matter (Nissenbaum and Kaplan, 1972) and evidence has been presented that the sul~~f~~phur content of the humic substances increases with degradation (Francois 1987). Concluding, it is here proposed that humic substances caused elevated S concentrations in the diagenetic calcite phase that occludes the skeletal pore space (Fig. 6D) and

causes the CLFM fluorescence in all three wavelengths (Blyth et al., 2008; Orland et al., 2009, 2012; Fig. 8).

Similarly, microtomographic data indicate the former presence of organic matter in dark triangular areas of rostra (Fig. 9) as observed in BSE images. The brightness of a carbonate observed in CT image indicates the degree of attenuation of an X-ray passing through this material (Mobilio et al., 2015). As the inner tri-radial structures of rostra appear darker in colour relative to the calcite phase fringing these structures, we suggest that the fringing phase is made of a denser calcite phase compared to the inner structure. That observation is in line with the observation of a low optical relief of these features (supplement Fig. 1A-B).

This tentative interpretation presented here with regard to belemnite rostra is arguably consistent with observations of 10-40% organic matrix in the *Sepia* cuttlebone (Birchall and Thomas, 1983; Florek et al., 2009). This is relevant as we suggest that the belemnite rostrum is structurally similar but not homologous (Fuchs 2012) to the *Sepia* cuttlebone with regard to the primary intra-skeletal porosity. Having said this, the presence of preserved organic matter in ancient biogenic carbonates particularly, intra-crystalline organic matter is not uncommon (Clark, 1999, 2005). Excess carbon observed for *Megateuthis* has been interpreted as evidence for a former organic matrix within these low-Mg calcite biominerals (Dunca et al., 2006). Similarly, Florek (2004) argued for an excess of carbon in the rostra of *Belemnopsis* and *Hibolites*. Summing up: Different lines of circumstantial evidence point to the presence of remnant organic matter within biominerals. These data require verification or rejection via the application of spatially highly resolved geochemical data. This work is presently iunder progress.

5. Conclusions

Formatted: No underline, Font color: Auto

Ultrastructural data documented here suggest that the calcitic rostra of Mesozoic belemnites yielded 50-90% primary porosity probably filled with body fluids and/or organic matter during the life time of the animal. Porosity was distributed throughout the rostrum as opposed to being limited to

the central apical area. The primary biogenic rostrum framework consists of triaxial branches and tetrahedrons of variable size forming a honeycomb-like network. This structure arguably combined mechanical stability with an energy-efficient biomineralization strategy.

The recognition of belemnite rostra as a highly porous structure requires a re-interpretation of the function of the rostrum as counterweight to the soft body and has implications for the swimming mode of belemnites. On the level of a working hypothesis, we argue that the low-porosity fabric found in fossil rostra collected in outcrops worldwide is the result of a syntaxial, early diagenetic cement phase that nucleated upon the surface of the biogenic framework and subsequently occluded the pore space. The possibility of gradual occlusion of skeletal porosity by remote biomineralization during later ontogenetic stages during the life of the animal is possible but seems unlikely at present.

If the here-presented concepts hold true, then these new findings have significant implications with regard to geochemical proxy data collected from fossil belemnite rostra. Specifically, the fact that rostra may consist of biogenic and abiogenic calcite phases formed at different times may explain the controversially low reconstructed seawater temperatures and the uncommonly high scatter of proxy data even from well-preserved rostra collected in the same stratigraphic interval. This is because seawater properties of surficial water masses, the habitat of nektobenthic belemnites, are recorded in the biogenic portions of the rostrum whereas the early diagenetic phase reflects cooler basinal bottom or marine pore water signatures. Findings presented here form a solid and well-constrained petrographic data set but one that must be verified by high-resolution geochemical data of all paragenetic calcite phases observed.

6. Acknowledgement

~~RH~~ We acknowledge~~s~~ M. Born, S. Schremmer, and T. Seemann for technical preparation of thin- and ultra thin-sections~~,~~. We thank all the private collectors that generously donated ~~their~~ material

Formatted: Justified

making this study possible (H. Schwandt, P. Girod, G. Grimmberger, J. Kalbe, M. Sowiak and others). We acknowledge the comments by the two journal reviewers I. Jarvis and D. Fuchs and the editorial handling by Brian Jones. ~~s improving an earlier version of that manuscript~~

Formatted: No underline, Font color: Auto

Formatted: No underline, Font color: Auto, Not Highlight

Formatted: No underline, Font color: Auto

7. References

Anderson, T.F., Popp, B.N., Williams, A.C., Ho, L.Z., Hudson, J.D., 1994. The stable isotopic records of fossils from the Peterborough Member, Oxford Clay Formation (Jurassic), UK: palaeoenvironmental implications. Journal of the Geological Society, London 151, 125-138.

Arkhipkin, A., Weis, R., Mariotti, N., Shcherbich, Z., 2015. "Tailed" Cephalopods. Journal of Molluscan Studies 81, 345-355.

Barbin, V., 1991. Fluctuation in shell composition in *Nautilus* (Cephalopoda, Mollusca): evidence from Cathodoluminescence. Lethaia 25, 391-400.

Barbin, V., 2013. Application of cathodoluminescence microscopy to recent and past biological materials: a decade of progress. Mineralogy and Petrology 107, 353-362.

Benito, M.I., Reolid, M., 2012. Belemnite taphonomy (Upper Jurassic, Western Tethys) part II: Fossil-diagenetic analysis including combined petrographic and geochemical techniques. Palaeogeography, Palaeoclimatology, Palaeoecology 358, 89-108.

Berner, R.A., Westrich, J.T., Graber, R., Smith, J., Martens, C.S., 1978. Inhibition of aragonite precipitation from supersaturated seawater: a laboratory and field study. American Journal of Science 278, 816-837.

Birchall, J.D., Thomas, N.L., 1983. On the architecture and function of cuttlefish bone. Journal of Materials Science 18, 2081-2086.

Bizikov, V.A., Arkhipkin, A.I., 1997. Morphology and microstructure of the gladius and statolith from the boreal Pacific giant squid *Moroteuthis robusta* (Oegopsida; Onychoteuthidae). Journal of Zoology 241, 475-492.

Formatted: Font: 11 pt, No underline, English (United Kingdom)

Formatted: Font: 11 pt, No underline, English (United States)

586 Blyth, A.J., Baker, A., Collins, M.J., Penkman, K.E.H., Gilmour, M.A., Moss, J.S., 2008. Molecular
587 organic matter in speleothems and its potential as an environmental proxy. Quaternary Science
588 Reviews 27, 905–921.
589 Chateigner, D., Hedegaard, C., Wenk, H.R., 2000. Mollusc shell microstructures and crystallographic
590 textures. Journal of Structural Geology 22, 1723-1735.
591 Chinzei, K., Seilacher, A., 1993. Remote Biomineralization I: Fill skeletons in vesicular oyster shells.
592 Neues Jahrbuch für Geologie und Paläontologie, Abhandlungen 190, 349-361.
593 Clark, II G.R., 1999. Organic matrix taphonomy in some molluscan shell microstructures.
594 Palaeogeography, Palaeoclimatology, Palaeoecology 149, 305-312.
595 Clark, II G.R., 2005. Organic matrix in the porifera and Cnidaria: déjà vu through a temporal
596 telescope. Geological society of America Abstracts with Program 37, 366.
597 Cochran, J.K., Landman, N.H., Turekian, K.K., Michard, A., Schrag, D.P., 2003. Paleoceanography of
598 the Late Cretaceous (Maastrichtian) Western Interior Seaway of North America: evidence from Sr
599 and O isotopes. Palaeogeography Palaeoclimatology Palaeoecology 191, 45-64.
600 Cochran, J.K., Kallenberg, K., Landman, N.H., Weinreb, D., Turekian, K.K., Beck, A.J., Cobban, W.A.,
601 2010. Effect of diagenesis on the Sr, O, and C isotope composition of Late Cretaceous Mollusks
602 from the Western Interior Seaway of North America. American Journal of Science 310, 69-88.
603 Coronado, I., Pérez-Huerta, A., Rodríguez, S., 2013. Primary biogenic skeletal structures in
604 Multithecopora (Tabulata, Pennsylvanian). Palaeogeography, Palaeoclimatology, Palaeoecology
605 386, 286-299.
606 Dunca, E., Doguzhaeva, L., Schöne, B.R., Schootbrugge, B. v.d., 2006. Growth patterns in rostra of the
607 Middle Jurassic belemnite *Megateuthis giganteus*: controlled by the moon? Acta Universitatis
608 Carolinae – Geologica 49, 107-117.
609 Dupraz, C., Reid, R.P., Braissant, O., Decho, A.W., Norman, R.S., Visscher, P.T., 2009. Processes of
610 carbonate precipitation in modern microbial mats. Earth-Science Reviews 96, 141-162.

Formatted: Font: 11 pt, No underline, English (United States)

Formatted: Font: 11 pt, No underline, German (Germany)

Dutton, A., Huber, B.T., Lohmann, K.C., Zinsmeister, W.J., 2007. High-Resolution Stable Isotope Profiles of a Dimitobelid Belemnite: Implications for Paleodepth Habitat and Late Maastrichtian Climate Seasonality. Palaios 22, 642–650.

Florek, M., Youn, H.S., Ro, C.U., Wierzbowski, H., Osán, J., Kazimierczak, W., Kuczumow, A., 2004. Investigation of chemical composition of belemnite rostra by synchrotron-based X-ray microfluorescence and diffraction and electron microprobe. Journal of Alloys and Compounds 362, 99-106.

Florek, M., Fornal, E., Gomez-Romero, P., Zieba, E., Paszkowicz, W., Lekki, J., Nowak, J., Kuczumow, A., 2009. Complementary microstructural and chemical analyses of *Sepia officinalis* endoskeleton. Materials Science and Engineering C 29, 1220-1226.

Francois, R., 1987. A study of sulphur enrichment in the humic fraction of marine sediments during early diagenesis. Geochimica et Cosmochimica Acta 51, 17–27.

Fuchs, D., 2012. The "rostrum"-problem in coleoid terminology – an attempt to clarify inconsistencies. Geobios 45, 29-39.

Goetz, A.J., Steinmetz, D.R., Griesshaber, E., Zaefferer, S., Raabe, D., Kelm, K., Irsen, S., Sehrbrock, A., Schmahl, W.W., 2011. Interdigitating biocalcite dendrites from a 3-D jigsaw structure in brachiopod shells. Acta Biomaterialia 7, 2237-2243.

Gröcke, D.R., Price, G.D., Ruffell, A.H., Mutterlose, J., Baraboschkin, E., 2003. Isotopic evidence for Late Jurassic-Early Cretaceous climate change. Palaeogeography, Palaeoclimatology, Palaeoecology 202, 97-118.

Guerra, A., 2006. Ecology of *Sepia officinalis*. Vie et Milieu – Life & Environment 56, 97-107.

Guzman, N., Ball, A.D., Cuif, J.-P., Dauphin, Y., Denis, A., Ortlieb, L., 2007. Subdaily growth patterns and organo-mineral nanostructure of the growth layers in the calcitic prisms of the shell of *Concholepas concholepas* Bruguière, 1789 (Gastropoda, Muricidae). Microscopy and Microanalysis 13, 397-403.

Formatted: Font: 11 pt, No underline, Font color: Auto

Formatted: Font: 11 pt, No underline, Font color: Auto, German (Germany)

Formatted: German (Germany)

Formatted: Font: 11 pt, No underline, German (Germany)

636 Huber, B.T., Hodell, D.A., 1996. Middle-Late Cretaceous climate of the Southern high latitudes: Stable
637 isotopic evidence for minimal equator-to-pole thermal gradients: Discussion and reply.
638 Geological Society of America Bulletin 108, 1193-1196.
639 Hückel, U., Hemleben, C., 1976. Diagenetische Spurenelement-Verschiebungen und Veränderungen
640 der Skelett-Strukturen bei Belemniten Rostren. Zentralblatt Geologie und Paläontologie Teil II
641 1976, 362-365.
642 Immenhauser, A., Schöne, B.R., Hoffmann, R., Niedermayr, A., 2016. Mollusc and brachiopod skeletal
643 hard parts: Intricate archives of their marine environment. Sedimentology 63, 1-59.
644 Jarvis, I., Trabucho-Alexandre, J., Gröcke, D., Uličný, D., Laurin, J., 2015. Intercontinental correlation
645 of organic carbon and carbonate stable isotope records: evidence of climate and sea-level change
646 during the Turonian (Cretaceous). The Depositional Record 1, 53-90.
647 Klug, C., Schweigert, G., Fuchs, D., Kruta, I., Tischlinger, H., 2015. Adaptations to squid-style high-
648 speed swimming in Jurassic belemnitids. Biological Letters 12, 1-5.
649 Kozdon, R., Kelly, D.C., Kita, N.T., Fournelle, J.H., Valley, J.W., 2011. Planktonic foraminiferal oxygen
650 isotope analysis by ion microprobe technique suggests warm tropical sea surface temperatures
651 during the Early Paleogene. Paleoceanography 26, 1-17.
652 Li, Q., 2011. Belemnite Palaeo-proxies and Dating of Mesozoic Carbonates. Ph.D. Thesis. 1-262,
653 Department of Earth Sciences, Univeristy College London.
654 Li, Q., McArthur, J.M., Atkinson, T.C., 2012. Lower Jurassic belemnites as indicators of palaeo-
655 temperature. Palaeogeography Palaeoclimatology, Palaeoecology 315, 38-45.
656 Li, Q., McArthur, J.M., Doyle, P., Janssen, N., Leng, M.J., Müller, W., Reboulet, S., 2013. Evaluating
657 Mg/Ca in belemnite calcite as a palaeo-proxy. Palaeogeography Palaeoclimatology,
658 Palaeoecology 388, 98-108.
659 Linzmeier, B.J., Kozdon, R., Peters, S.E., Valley, J.W., 2016. Oxygen isotope variability within *Nautilus*
660 shell growth bands. PLoS ONE (Accepted).

Formatted: Font: 11 pt, No underline, English (United Kingdom)

661 Longinelli, A., Iacumin, P., Ramigni, M., 2002. $\delta^{18}O$ of carbonate, quartz and phosphate from
662 belemnite guards: implications for the isotopic record of old fossils and the isotopic composition
663 of ancient seawater. Earth and Planetary Science Letters 203, 445-459.
664 Longinelli, A., Wierzbowski, H., Matteo, A. di, 2003. $\delta^{18}O(PO_4^{3-})$ and $\delta^{18}O$(CO32-) from belemnite
665 guards from Eastern Europe: implications for palaeoceanographic reconstructions and for the
666 preservation of pristine isotopic values. Earth and Planetary Science Letters 209, 337-350.
667 Lowenstam, H.A., Weiner, S., 1989. On Biomineralization. Oxford University Press, New York 324 pp.
668 Lukeneder, A., Harzhauser, M., Müllegger, S., Piller, W.E., 2010. Ontogeny and habitat change in
669 Mesozoic cephalopods revealed by stable isotopes ($\delta^{18}O$, $\delta^{13}C$). Earth and Planetary Science
670 Letters 296, 103-114.
671 Massonne, H.-J., Neuser, R.D., 2005. Ilmenite exsolution in olivine from the serpentinite body at
672 Zöblitz, Saxonian Erzgebirge – microstructural evidence using EBSD. Mineralogical Magazine 69,
673 119-124.
674 McArthur, J.M., Janssen, N.M.M., Reboulet, S., Leng, M.J., Thirlwall, M.F., Schootbrugge, B. v.d.,
675 2007. Palaeotemperatures, polar ice-volume, and isotope stratigraphy (Mg/Ca, $\delta^{18}O$, $\delta^{13}C$,
676 $^{87}Sr/^{86}Sr$): The Early Cretaceous (Berriasian, Valanginian, Hauterivian). Palaeogeography
677 Palaeoclimatology, Palaeoecology 248, 391-430.
678 Mobilio, S., Boscherini, F., Meneghini, C., 2015. Synchrotron Radiation: Basics, Methods and
679 Applications. Springer Berlin Heidelberg.
680 Mokso, R., Marone, F., Irvine, S., Nyvlt, M., Schwyn, D., Mader, K., Taylor, G.K., Krapp, H.G., Skeren,
681 M., Stampanoni, M., 2013. Advantages of phase retrieval for fast X-ray tomographic microscopy.
682 Journal of Physics D: Applied Physics 46, 1-12.
683 Müller-Stoll, H., 1936. Beiträge zur Anatomie der Belemnoidea. Nova Acta Leopoldina-Abhandlungen
684 der Kaiserlich Leopoldinisch-Carolinisch Deutschen Akademie der Naturforscher, Neue Folge 4, 1-
685 70.

Formatted: Font: 11 pt, No underline, Font color: Auto, English (United States)

Formatted: Font: 11 pt, No underline, Font color: Auto, English (United States)

686 Neuser, R.D., Bruhn, F., Götze, J., Habermann, D., Richter, D.K., 1996. Kathodolumineszenz: Methodik
687 und Anwendung. Zentralblatt Geologie und Paläontologie Teil 1 1995, 287-306.
688 Niebuhr, B., 1995. Fazies-Differenzierungen und ihre Steuerungsfaktoren in der höheren Oberkreide
689 von S-Niedersachsen/Sachsen-Anhalt (N-Deutschland). Berliner Geowissenschaftliche
690 Abhandlungen, Reihe A 174, 1-131.
691 Niebuhr, B., Hiss, M., Kaplan, U., Tröger, K.A., Voigt, S., Voigt, T., Wiese, F., Wilmsen, M., 2007.
692 Lithostratigraphie der norddeutschen Oberkreide. Schriftenreihe der Deutschen Gesellschaft für
693 Geowissenschaften 55, 1-136.
694 Nissenbaum, A., Kaplan, I.R., 1972. Chemical and isotopic evidence for the *in situ* origin of marine
695 humic substances. Limnology and Oceanography 17, 570-582.
696 Orland, I.J., Bar-Matthews, M., Kita, N.T., Ayalon, A., Matthews, A., & Valley, J.W., 2009. Climate
697 deterioration in the Eastern Mediterranean as revealed by ion microprobe analysis of a
698 speleothem that grew from 2.2 to 0.9 ka in Soreq Cave, Israel. Quaternary Research 71, 27–35.
699 Orland, I.J., Bar-Matthews, M., Ayalon, A., Matthews, A., Kozdon, R., Ushikubo, T., Valley, J.W., 2012.
700 Seasonal resolution of Eastern Mediterranean climate change since 34 ka from a Soreq Cave
701 speleothem. Geochimica et Cosmochimica Acta 89, 240–255.
702 Oti, M.N., Ogbuji, L.U., Breuer, K.H., 1989. Diagenetic transformation of magnesium calcite in a
703 monocrystalline rock-forming carbonate skeleton of an echinoderm. Chemical Geology 76, 303-
704 308.
705 Parkinson, D., Curry, G.B., Cusack, M., Fallick, A.E., 2005. Shell structure, patterns and trends of
706 oxygen and carbon stable isotopes in modern brachiopod shells. Chemical Geology 219, 193-235.
707 Podlaha, O.G., Mutterlose, J., Veizer, J., 1998. Preservation of $\delta^{18}O$ and $\delta^{13}C$ in belemnite rostra from
708 the Jurassic/Early Cretaceous successions. American Journal of Science 298, 324-347.
709 Price, G.D., Page, K.N., 2008. A carbon and oxygen isotopic analysis of molluscan faunas from the
710 Callovian-Oxfordian boundary at Redcliff Point, Weymouth, Dorset: implications for belemnite
711 behaviour. Proceedings of the Geologists´ Association 119, 153-160.

Formatted: Font: 11 pt, No underline, Font color: Auto, English (United States)

712 Price, G.D., Sellwood, B.W., 1997. “Warm” palaeotemperatures fron high Late Jurassic
713 palaeolatitudes (Falkland Plateau): Ecological, environmental or diagenetic controls?
714 Palaeogeography Palaeoclimatology, Palaeoecology 129, 315-327.
715 Price, G.D., Wilkinson, D., Hart, M.B., Page, K.N., Grimes, S.T., 2009. Isotopic analysis of coexisting
716 Late Jurassic fish otoliths and molluscs: Implications for upper-ocean water temperature
717 estimates. Geology 37, 215-218.
718 Price, G.D., Fözy, I., Janssen, N.M.M., Pálfy, J., 2011. Late Valanginian-Barremian (Early Cretaceous)
719 palaeotemperatures inferred from belemnite stable isotope and Mg/Ca ratios from Bersek
720 Quarry (Gerecse Mountains, Trandanubian Range, Hungary). Palaeogeography
721 Palaeoclimatology, Palaeoecology 305, 1-9.
722 Price, G.D., Hart, M.B., Wilby, P.R., Page, K.N., 2015. Isotopic analysis of Jurassic (Callovian) molluscs
723 from the Christian Malford Lagerstätte (UK): Implications for ocean water temperature estimates
724 based on belemnoids. Palaios 30, 645-654.
725 Richter, D.K., Götte, T., Götze, J., Neuser, R.D., 2003. Progress in application of cathodoluminescence
726 (CL) in sedimentary petrology. Mineralogy and Petrology 79, 127-166.
727 Richter, D.K., Neuser, R.D., Schreuer, J., Gies, H., Immenhauser, A., 2011. Radiaxial-fibrous calcites: a
728 new look on an old problem. Sedimentary Geology 239, 23-36.
729 Ritter, A.-C., Kluge, T., Berndt, J., Richter, D.K., John, C.M., Bodin, S., Immenhauser, A., 2015.
730 Application of redox sensitive proxies and carbonate clumped isotopes to Mesozoic and
731 Palaeozoic radiaxial fibrous cements. Chemical Geology 417, 306-321.
732 Ritter, A.-C., Mavromatis, V., Dietzel, M., Wiethoff, F., Griesshaber, E., Casella, L., Schmahl, W.,
733 Koelen, J., Neuser, R.D., Leis, A., Buhl, D., Niedermayr, A., Bernasconi, S.M., Immenhauser, A.
734 (submitted). Experimental diagenesis: I – Exploring the impact of diagenesis on (isotope)
735 geochemical and microstructural features in biogenic aragonite. Geochimica et Cosmochimica
736 Acta.

737 Rosales, I., Quesada, S., Robles, S., 2001. Primary and diagenetic isotopic signals in fossils and
738 hemipelagic carbonates: the Lower Jurassic of northern Spain. Sedimentology 48, 1149-1169.
739 Rosales, I., Quesada, S., Robles, S., 2004a. Paleotemperature variations of Early Jurassic seawater
740 recorded in geochemical trends of belemnites from the Basque-Cantabrian basin, northern Spain.
741 Palaeogeography, Palaeoclimatology, Palaeoecology 203, 253-275.
742 Rosales, I., Robles, S., Quesada, S., 2004b. Elemental and oxygen isotope composition of Early
743 Jurassic Belemnites: Salinity vs. Temperature signals. Journal of Sedimentary Research 74, 342-
744 354.
745 Saelen, G., 1989. Diagenesis and construction of the belemnite rostrum. Palaeontology 32, 765-798.
746 Seilacher, A., Chinzei, K., 1993. Remote Biomineralization 2: Fill skeletons controlling buoyancy in
747 shelled cephalopods. Neues Jahrbuch für Geologie und Paläontologie, Abhandlungen 190, 363-
748 373.
749 Sessa, J.A., Larina, E., Knoll, K., Garb, M., Cochran, J.K., Huber, B.T., MacLeod, K.G., Landman, N.H.,
750 2015. Ammonite habitat revealed via isotopic composition and comparisons with co-occurring
751 benthic and planktonic organisms. Proceedings of the National Academy of Sciences of the
752 United States of America 112, 15562-15567.
753 Sherrard, K.M., 2000. Cuttlebone Morphology Limits Habitat Depth in Eleven Species of *Sepia*
754 (Cephalopoda: Sepiidae). Biological Bulletin 198, 404-414.
755 Spaeth, C., 1971. Aragonitische und calcitische Primärstrukturen im Schalenbau eines Belemniten aus
756 der englischen Unterkreide. Paläontologische Zeitschrift 45, 33-40.
757 Spaeth, C., 1973. Weitere Untersuchungen der Primär- und Fremdstrukturen in calcitischen und
758 aragonitischen Schalenlagen englischer Unterkreide-Belemniten. Paläontologische Zeitschrift 47,
759 163-174
760 Spaeth, C., 1975. Zur Frage der Schwimmverhältnisse bei Belemniten in Abhängigkeit vom
761 Primärgefüge der Hartteile. Paläontologische Zeitschrift 49, 321-331.

Formatted: Font: 11 pt, No underline, Font color: Auto, English (United States)

762 Stevens, G.R., 1965. The Jurassic and Cretaceous Belemnites of New Zealand and a Review of the
763 Jurassic and Cretaceous Belemnites of the Indo-Pacific Region. New Zealand Geological Survey
764 Paleontological Bulletin 36, 1-283.
765 Swart, P.K., 2015. The geochemistry of carbonate diagenesis: The past, present and future.
766 Sedimentology 62, 1233-1304.
767 Ullmann, C.V., Korte, C., 2015. Diagenetic alteration in low-Mg calcite from macrofossils: A review.
768 Geological Quarterly 59, 3-20.
769 Ullmann, C.V., Frei, R., Korte, C., Hesselbo, S.P., 2015. Chemical and isotopic architecture of the
770 belemnite rostrum. Geochemica et Cosmochimica Acta 159, 231-243.
771 Ullmann, C.V., Thibault, N., Ruhl, M., Hesselbo, S.P., Korte, C., 2014. Effect of a Jurassic oceanic
772 anoxic event on belemnite ecology and evolution. Proceedings of the National Academy of
773 Sciences of the United States of America 111, 10073-10076.
774 Urey, H.C., Lowenstein, H.A., Epstein, S., McKinney, C.R., 1951. Measurements of paleotemperatures
775 and temperatures of the upper Cretaceous of England, Denmark, and the southern United States.
776 Bulletin of the Geological Society of America 62, 399-416.
777 Veizer, J., 1974. Chemical diagenesis of belemnite shells and possible consequences for
778 paleotemperature determination. Neues Jahrbuch für Geologie und Paläontologie,
779 Abhandlungen 147: 91-111.
780 Visscher, P.T., Stolz, J.F., 2005. Microbial mats as bioreactors: populations, processes and products.
781 Palaeogeography, Palaeoclimatology, Palaeoecology 219, 87-100.
782 Voigt, S., Wilmsen, M., Mortimore, R.N., Voigt, T., 2003. Cenomanian palaeotemperatures derived
783 from the oxygen isotopic composition of brachiopods and belemnites: evaluation of Cretaceous
784 palaeotemperature proxies. International Journal of Earth Sciences (Geologische Rundschau) 92,
785 285-299.
786 Wanamaker, A.D., Baker, A., Butler, P.G., Richardson, C.A., Scourse, J.D., Ridgway, I., Reynolds, D.J.,
787 2009. A novel method for imaging internal growth patterns in marine mollusks: A fluorescence

Formatted: Font: 11 pt, No underline, Font color: Auto, English (United Kingdom)

788 case study on the aragonitic shell of the marine bivalve *Arctica islandica* (Linnaeus). Limnology
789 and Oceanography: Methods 7, 673-681.
790 Weiner, S., Addadi, L., 2011. Crystalization Pathways in Biomineralization. Annual Review of Materials
791 Research 41, 21-40.
792 Wierzbowski, H., 2004. Carbon and oxygen isotope composition of Oxfordian-Early Kimmeridgian
793 belemnite rostra: palaeoenvironmental implications for Late Jurassic seas. Palaeogeography,
794 Palaeoclimatology, Palaeoecology 203, 153-168.
795 Wierzbowski, H., Joachimski, M.M., 2007. Reconstruction of late Bajocian-Bathonian marine
796 palaeoenvironments using carbon and oxygen isotope ratios of calcareous fossils from the Polish
797 Jura chain (central Poland). Palaeogeography, Palaeoclimatology, Palaeoecology 254, 523-540.
798 Wierzbowski, H., Joachimski, M.M., 2009. Stable Isotopes, Elemental Distribution, and Growth Rings
799 of Belemnopsid Belemnite Rostra: Proxies for Belemnite Life Habitat. Palaios 24, 377-386.
800 Zachos, J., Pagani, M., Sloan, L., Thomas, E., Billups, K., 2001. Trends, Rhythms, and aberrations
801 inglobal climate 65 Ma to present. Science 292, 686-693.
802
803
804
805
806
807
808
809
810

Figure captions

Fig. 1A-B) Structural and ultrastructural composition of belemnite rostra. *Belemnitella mucronata*, thin sections photographed under crossed polarizers. A) Cross section with pseudo-uniaxial cross indicating radially arranged calcite fibres, red box refers to C. B) Longitudinal section with central apical line and radiating fibres from the centre to the margin, stippled line refers to the position of cross section shown in A. C) Idealized bundle of calcite fibres, each fibre contains a stack of tetrahedral elements. D) SEM BSD image of the tetrahedral ultrastructure of *Megateuthis gigantea*, dashed lines (I-IV) indicate section planes and corresponding reconstructions. Primary skeletal framework is shown in blue, yellow and green whilst early diagenetic phase is shown in white and red for the crystal boundaries. The basis of tetrahedrons points toward the centre of the belemnite rostrum and its tip towards the rostrum margin i.e. the growth direction. E) Three dimensional reconstruction of a single tetrahedron of the belemnite endoskeleton. F) Reconstruction of the complex spatial arrangement of biogenic and early diagenetic phases. Colour code in lower right. G) SEM image of a single complex tetrahedron (black line) with indication of structural elements. Primary skeletal components: br = branch, trc = triradial centre, rf = reinforcement, ic = isopachous crystallites. **(full page width; bw in print, colour in pdf)**

Fig. 2A-B) SEM BSD images of *Megateuthis gigantea*. A-B) Section perpendicular to the c-axes of calcite fibres (section plane II in Fig. 1D-II). White stippled line indicate dissolution features (early diagenetic), black stippled line indicate microstylolites ~~(late diagenetic)~~. **(full page width; bw in print, colour in pdf)**

Fig. 2A-B) SEM BSD images of *Megateuthis gigantea*. A-B) Section perpendicular to the c-axes of calcite fibres (section plane II in Fig. 1D-II). Blue stippled line indicate dissolution features (early diagenetic), red stippled line indicate microstylolites ~~(late diagenetic)~~. **(full page width; bw in print, colour in pdf)**

Fig. 3A-F) SEM BSD images of *Megateuthis gigantea*. A-E) Section perpendicular to the c-axes of calcite fibres. A) Triangular structures with a relatively thick outer, light grey margin of abiogenic early diagenetic cement and a small darker centre with branches giving rise to reinforcement structures representing the primary biogenic skeletal framework. B) Larger dark grey, organic rich triangular elements belonging to the biogenic skeletal framework, partly with light grey central abiogenic calcite filling of variable sizes. Branches are often short and cut off at variable distances from the centre. C) Some smaller and a few larger biogenic skeletal elements with cut off branches (lower arrow) and reinforcement structures (upper arrow). Note the variable expression of early diagenetic crystallites with sheaths of remnant organic matter. D) Close up of larger, biogenic skeletal elements and abiogenic isopachous calcites coated by remnants of organic matter within the brighter outer margin. Central portion of the biogenic skeletal elements shows abiogenic crystal; arrows point to dissolved branches. E) Centre of biogenic skeletal element completely filled with abiogenic bright calcite leaving only a thin dark inner margin. F) Same specimen, section subparallel to the c-axes showing a homogenous central portion ("trunk" – white line) of pyramidal morphology rich in intracrystalline organic matter surrounded by inclined isopachous calcite crystals coated by remnants of organic matter. This overall pattern results in a~~n~~ "~~x~~Christmas~~ mas~~ tree like" structure (compare with Fig. 1D). **(full page width; bw in print and pdf)**

Fig. 4A-E) *Megateuthis gigantea*, EBSD map with colour code in sections perpendicular to the c-axes of the fiber bundles. Same colours represent same crystallographic orientations. In A and B angular deviation from blue to red is up to 40°, in D angular deviation is 2°. A) Overview map showing the bundling of fibres with identical orientation of a-axes, black frame indicates area for close up in B; blue frame refers to Fig. 5A-C. B) Close up map, within one bundle blue tinted fibres are mainly neighboured by other blue fibres, red tinted fibres are surrounded by red fibres. C) Close up ~~to demonstrate slight~~ documenting minor angular deviation within one fibre (compare with D). D) Map of a single fibre with an angular deviation of 2° from blue to red, showing a slight systematic shift of axes orientation. E) Pole-plots of c-axes {001} and a-axes {010} from all fibres shown in A, all c-axes show nearly the same orientation while the a-axes demonstrate the bundled structure of the rostral fabric which may have improved the stability of the skeletal structure. **(full page width; bw in print, colour in pdf)**

Fig. 5A-F) Transmitted light, polarized light and cathodoluminescence. Thin section of *Megateuthis gigantea*, A-C refer to the blue frame in Fig. 4A, D-F are close ups (black frame in A) A and D) TL image perpendicular to the c-axes of calcite fibres, filigree biogenic skeletal framework is indicated by the dark tinted structures, primary porosity is represented by the abiogenic translucent calcites. Note banded distribution of calcite fibre domains relating to larger and smaller organic-rich biogenic skeletal elements, single fibres may contain a central portion of transparent calcite of varying size, bundling of adjacent calcite fibres is indicated by the same orientation of the triangles. B and E) Uniform extinction (orientation) of adjacent fibres under crossed polarizers. C and F) CL of abiogenic calcite portions show a dark blue, intrinsic luminescence (pure stoichiometric calcite), CL of the biogenic skeletal framework show light blue luminescence. **(full page width; bw in print, colour in pdf)**

Fig. 6) Electron microprobe data for *Megateuthis gigantea*. A) Overview BSE map B) Shows higher Mg concentrations within the triangular areas dark in BSE images and a lower Mg concentration in the surrounding area bright in BSE images. C) Shows higher P concentrations within the triangular areas dark in BSE images and a lower P concentration in the surrounding area bright in BSE images. D) Shows lower S concentrations within the triangular areas dark in BSE images and higher S concentrations in the surrounding region bright in BSE images. **(full page width; bw in print, colour in pdf)**

Fig. 7) Fluorescence microscope images for *Megateuthis gigantea*. A) Transmitted light shows brownish triangular structures, rich in organic matter and dark in BSE images, partly with central translucent areas (compare with Fig. 1D section plane IV, Fig. 3D, E, 5A, D). B) Shows brighter fluorescent triangular area compared to the in transmitted light translucent calcite. **(full page width; bw in print, colour in pdf)**

Fig. 8) Confocal laser fluorescence microscopy images of *Megateuthis gigantea*. A) CLFM images showing fluorescence in far-red light (λ = 664 to 696 nm). B) CLFM images showing fluorescence in visible green light (λ = 505 to 539 nm). C and D) CLFM images showing fluorescence in visible red light (λ = 589 to 621 nm). Triangular structures visible in other imaging techniques (Fig. 3, 5-7) do not fluoresce as brightly as cracks (B) or early diagenetic calcite (Fig. 3) separating the triangles (A, B, C, D). D) Higher magnification shows some brighter fluorescing calcite between the triangular elements dark in BSE images (Fig. 1, 3). Brightly fluorescent early diagenetic calcite separating triangles ~~also contains~~is enriched in ~~elevated~~ S (Fig. 6~~),~~). ~~which may support inclusion of S-rich humic substances as the cause of fluorescence.~~ **(full page width; bw in print, colour in pdf)**

Fig. 9) Three-dimensional visualization of the filigree biogenic framework. Synchrotron radiation based tomographic visualization of a sub-volume of the rostrum of *Megateuthis gigantea*. Specimen was scanned with an isotropic voxel size of 0.74µm. A) Multi-planar image of a sub-domain of the original dataset with dimensions of 447x592x663 voxels, triangular elements dark in BSE images appear here as dark elements due to reduced densities. B-D) Volumetric renderings of the same sub-domain with variable rendering settings. **(full page width; bw in print, colour in pdf)**

Formatted: Justified

Supplementary Figures

Formatted: Justified

Fig. 1) Examples of the filigree framework from other belemnite species. A-B) *Gonioteuthis quadrata*, A) shows the Becke line outside of the triangular area with a relatively larger distance between the sample and objective. B) ~~Shows~~ Image shows the Becke line within the triangular area while the distance between the sample and the objective was reduced, accordingly the triangular area (dark in BSE; ~~(~~Fig. 3~~)~~) has a lower optical relief. C-D) *Belemnitella mucronata*, C) thin section under polarized light, D) same area under CL showing microfractures filled with Mn-rich calcite tracing the outline of triangular elements (encircled). **(full page width; bw in print, colour in pdf)**

Fig. 2) SEM BSD images of *Megateuthis gigantea*. A-F) Section plane parallel to the c-axes of calcite fibres. A-C) stepwise enlargement of a particular area. D-F) stepwise enlargement of a particular area. A and D give the impression of a concentric arrangement of distinct darker and brighter layers (black frames enlarged in B and E), arrow in D point to an organic rich layer (laminae obscura sensu Müller-Stoll, (1936)). B and E) Allow the recognition of single darker structures of tetrahedral morphology with their tips pointing towards the outer margin of the belemnite rostrum, i.e. the growth direction (black frames enlarged in C and F). C and F) show the intricate framework of biogenic (dark) and abiogenic (light) carbonate phase within the rostrum, larger dark grey, triangular elements belonging to the biogenic skeletal framework, partly with light grey central abiogenic calcite filling of variable size. **(full page width; bw in print, colour in pdf)**

Evidence for a composite organic-inorganic fabric of belemnite rostra: Implications for palaeoceanography and palaeoecology

Hoffmann, R.[1], Richter, D.K.[1], Neuser, R.D.[1], Jöns, N.[1], Linzmeier, B.J.[2], Lemanis, R.E.[1], Fusseis, F.[3], Xiao, X.[4] and Immenhauser A[1]

[1] Department of Earth Sciences, Institute of Geology, Mineralogy, and Geophysics; Ruhr-Universität Bochum, Universitätsstrasse 150, 44801 Bochum, Germany

Corresponding author. E-mail address: rene.hoffmann@rub.de (R. Hoffmann), phone number: +49-234-3227769

[2] Department of Geoscience, University of Wisconsin – Madison, 1215 West Dayton St, Madison, Wisconsin, USA

[3] School of Geosciences, The University of Edinburgh, Grant Institute, King's Buildings, West Mains Road, Edinburgh, UK EH9 3JW

[4] Advanced Photon Source, Argonne National Laboratory, 9700 S. Cass Ave., Lemont, IL, 60439 USA.

Abstract

Carbonate skeletons of fossil marine organisms are widely used to reconstruct palaeoceanographic parameters. Specifically, the geochemistry of Jurassic and Cretaceous belemnite rostra is traditionally interpreted to represent near sea-surface seawater properties. More recently, an increasing number of workers, have reported significant scatter in geochemical data (e.g., $\delta^{18}O$, $\delta^{13}C$, element/Ca ratio) when comparing rostra from the same stratigraphic level or within a single belemnite rostrum. This scatter is not explained by differential diagenetic overprint alone. Here we report petrographic evidence on the primary ultrastructure of rostra of *Megateuthis* (Middle Jurassic) and *Belemnitella* and *Gonioteuthis* (Late Cretaceous). The biogenic ultrastructure consists of a filigree framework of triaxial branches and tetrahedrons of variable size forming a honeycomb-like network. Data presented here suggest that these rostra yielded as much as 50 to 90% primary pore space. On the level of a working hypothesis - and in analogy with modern cephalopods - we propose that the pore space was formerly filled with body fluid and/or organic compounds during the life time of these organisms. Intra-rostral porosity was post mortem occluded by earliest diagenetic isopachous calcite cements of a non-biogenic origin. These may have been precipitated due to increased alkalinity related to the decay of organic matter. If this holds true, then the resulting fabric represents a composite biogenic/abiogenic structure. In order to optically separate the two calcite phases forming a single calcite fibre, we employed a wide range of state-of-the-art analytical tools to thin sections and ultra-thin sections of well-preserved specimens. Pending a verification of these well-supported ultrastructural data by means of high-resolution geochemical analyses from biogenic and abiogenic phases, we suggest that these findings have significance for those using belemnite rostra as archives of their palaeoenvironment.

Keywords: belemnite, ultrastructure, carbonate archive, diagenesis, Jurassic-Cretaceous

1. Introduction

The ultrastructure of recent biogenic carbonates is of great interest for those concerned with biomineralization research in general (Weiner and Addadi, 2011; Goetz et al., 2011), those studying the primary biogenic skeletal structures of fossil skeletal hardparts (e.g., Coronado et al., 2013), and for palaeoceanographers exploring these materials for their bearing on past climate dynamics (Saelen, 1989; Cochran et al., 2003; Parkinson et al., 2005; Jarvis et al., 2015; Immenhauser et al., 2016). Whereas the tests of planktonic and benthic foraminifera and coccoliths are important archives of open marine environments throughout the Cenozoic and beyond (e.g., Zachos et al., 2001), much of what is known about Cretaceous and Jurassic palaeoceanography has been deduced from the geochemical archive of the calcareous rostra of extinct cephalopods, specifically belemnites (Dutton et al., 2007). Reasons for the wide use of these archive materials include their abundance in the fossil record, the diagenetically stable low-Mg calcite mineralogy of rostra (Veizer, 1974; Saelen, 1989), and the broad palaeobiogeographic distribution of belemnites in the marine Boreal and Tethyan realms, (e.g., Urey et al., 1951; Voigt et al., 2003; Wierzbowski, 2004; McArthur et al., 2007; Dutton, 2007; Price and Page, 2008; Wierzbowski and Joachimski, 2009; Price et al., 2009 2011; Li et al., 2012, 2013). As with all biogenic carbonates, however, these archives undergo post mortem diagenetic alteration, representing a major obstacle in carbonate research (Swart, 2015).

Characteristic geochemical patterns and fabrics in biogenic carbonate hardparts have been used to test for example molluscs (e.g., Cochran et al., 2003, Sessa et al., 2015, Immenhauser et al., 2016), brachiopods (Parkinson et al., 2005), or foraminifera (e.g., Huber and Hodell, 1996; Kozdon et al., 2011) for evidence of diagenetic alteration. In the case of ammonites, the degree of preservation of nacre tablets provides evidence with regard to the preservation of these exoskeletons, to name one example (e.g., Cochran et al., 2010). With regard to belemnite rostra, the observation of an intact fibrous microfabrics in thin sections and polished rock surfaces in combination with cathodoluminescence is commonly used to identify well-preserved belemnite rostra (Rosales et al., 2001). In contrast, cloudy areas, exfoliation, fractures, stylolites, or boring traces are interpreted as

79 evidence for post mortem alteration (Saelen, 1989; Li, 2011; Benito and Reolid, 2012). A rigorous
80 discussion of screening techniques, including trace-element concentrations, and isotopic ratios
81 applied to biogenic low-Mg calcite macrofossils, has been provided by Ullmann and Korte (2015).
82 Similarly, a “best practice” approach for the interpretation of mollusc and brachiopod carbonate
83 archives was presented by Immenhauser et al. (2016).

84 The ultrastructure of belemnite rostra was first studied by Müller-Stoll (1936). This author
85 described organic-rich (laminae obscura) and carbonate-rich (laminae pellucidae) concentric growth
86 rings. Both of these were later shown to be calcitic but differ due to variable amounts of occluded
87 organic matter (Saelen, 1989). Growth rings are made up by fibrous calcite crystals radiating from a
88 central zone called apical line (Richter et al., 2011) forming what seems to be a low-porosity fabric
89 (Saelen, 1989 and references therein; Fig. 1A-C). Single fibres (= radial structures of Saelen, 1989) can
90 be arranged in bundles traversing the concentric growth layers. Each fibre thickens outwards and
91 shows a sub-fibrous framework potentially first proposed - but not further explored - by Saelen
92 (1989, Fig. 15a).

93 Belemnites are traditionally considered to secrete their endoskeleton in oxygen isotope
94 equilibrium with ambient seawater (e.g., Anderson et al., 1994; Price and Sellwood, 1997; Voigt et
95 al., 2003; Price et al., 2009; Wierzbowski and Joachimski, 2007, 2009). The main argument brought
96 forward is commonly the presence of what are considered cyclical oxygen isotope patterns
97 interpreted as seasonal seawater temperature variations (Urey et al., 1951). The PeeDee belemnite
98 used in Urey´s study was considered as well-preserved based on the compact fabric and the optical
99 features of the calcite crystals (but see Li, 2011 for discussion). The assumption of equilibrium
100 precipitation was further supported by data sets from recent cephalopods including *Nautilus*, *Sepia*,
101 and *Spirula* precipitating their skeletal hardparts in near-equilibrium with $\delta^{18}O_{seawater}$ (Lukeneder et
102 al., 2010). In contrast to this traditional view, there is an increasing amount of evidence suggesting
103 that belemnite rostra are problematic archives of their palaeoenvironment (see Immenhauser et al.,
104 2016 for detailed discussion). For example, Price et al. (2015) reported an offset of about 5°C

between the aragonitic phragmocone and the calcitic rostrum of a single specimen of *Cylindroteuthis*. This offset was regarded as vital effect but it remains unclear whether the temperatures derived from the aragonite are too warm or from the calcite too cool. Similarly, high intra-rostral variability of elemental (Ca, Mn, Mg, Fe, Sr) and isotopic ($\delta^{18}O$, $\delta^{13}C$) composition, the latter with a scatter of up to 2‰, has been reported from belemnite rostra lacking evidence for diagenetic alteration (Podlaha et al., 1998).

The significant discrepancy of these data sets forms a strong motivation for a reconsideration of belemnite rostra as archives of their palaeoenvironment. Here, we report data from a wide set of state-of-the-art analytical infrastructure applied to thin- and ultra-thin sections of exceptionally well-preserved Jurassic and Cretaceous belemnite rostra. The following aims guided this paper: First, to present well-constrained petrographic evidence for the complex primary biogenic framework of these rostra; second, to document evidence that points to the highly porous nature of this biogenic framework; third, to assess the relative proportion between primary skeleton and porosity; fourth, to discuss the timing and nature of the pore-filling calcites phase. Evidence reported here has significance for the interpretation of proxy data from ancient belemnite rostra and forms the foundation of a detailed, high-resolution geochemical study that will be in the focus of forthcoming work.

2. Materials and Methods

2.1. Belemnites

Thin sections (30 µm) and ultra-thin sections (< 10 µm) of two well-preserved orthorostra of *Megateuthis gigantea* (Schlotheim, 1820) from the Middle Jurassic and one specimen of *Belemnitella mucronata* (Schlotheim, 1813) and *Gonioteuthis quadrata* (Blainville, 1827) from the Upper Cretaceous were studied. Specimens of *Megateuthis* were collected in Bajocian marly limestone deposits from southern Germany. *Belemnitella* rostra are from the late early Campanian (*mucronata*

Zone), and *Gonioteuthis* from the early Campanian *lingua*/*quadrata* – *gracilis*/*mucronata* Zone from northwestern Germany. *Gonioteuthis* and *Belemnitella* rostra were embedded in calcareous (65-90%) epicontinental shelf deposits of the Misburg Formation (Niebuhr, 1995; Niebuhr et al., 2007). Specimens did not display evidence for exfoliation nor did they show boring traces of the surfaces of rostra. Specimens were sectioned along their long axis in a marginal position and perpendicular to the c-axis of their calcite fibres. One section cuts the rostrum of *Megateuthis* perpendicular to the long axis.

2.2. Methods

Surfaces of thin sections were chemo-mechanically etched using colloidal silica (OP-S) for 5-15 minutes to reduce surface irregularities on an atomic scale (Massonne and Neuser, 2005) and coated by a thin carbon layer. All coated thin sections have been studied under a high-resolution field emission scanning electron microscope (HR-FESEM) type LEO/ZEISS 1530 Gemini using a backscatter detector (BSD) at the Ruhr-Universität Bochum, Germany (Figs. 1-3).

Crystallographic orientation of belemnite calcite fibres was determined by electron backscattered diffraction (EBSD; Nordlys, OXFORD Instruments). The data acquisition and analysis was performed using the software packages AZtec and Channel 5 by Oxford Instruments (Fig. 4). The scanning electron microscope (SEM) was operated at beam energy of 20 kV, an aperture of 60 µm, a working distance of 25 mm and a tilt angle of 70°. Thin sections were mapped at Bochum University in the high-resolution mode using a grid matrix (1149x748 points) at a step width of 2.017 µm (Fig. 4A) and (543x266 points) at a step width of 1.652 µm (Fig. 4D) and for the single calcite fibre 50 µm to reduce artefacts and increase the reliability of the data. The orientations of the crystals in the individual maps were visualized using a rainbow colour coding ranging from blue over green and yellow to orange and red, where identical colours indicate identical crystal axis orientations. For visualizing the weak angular deviations in the crystal lattice in a single calcite fibre, we applied an

157 angular resolution of 2 degrees for the complete rainbow colour range. In addition, orientations of
158 the measured crystallographic axes were plotted into the lower hemisphere of a Schmidt net (Fig.
159 4E).

160 Rostra were further investigated under a cathodoluminescence microscope type HC1-LM by
161 Lumic equipped with a hot cathode (Neuser et al., 1996) and a digital camera system (DP73 by
162 Olympus) for recording digital images at Bochum. Beam energy of 14kV and a beam current density
163 between 5 and 10 μA/mm² were generally used for the CL-measurements. Integration times for CL-
164 spectra were commonly between 10 and 60 seconds (Fig. 5).

165 X-ray element distribution maps were acquired using a Cameca SX5FE field emission electron
166 microprobe at Bochum. The acceleration voltage was 15 keV with a probe current of about 80 nA and
167 a fully focused beam. The intensity of S Kα1 was recorded simultaneously on two wavelength
168 dispersive spectrometers equipped with LPET and PET analyzing crystals. The Mg Kα1 line was also
169 measured on two spectrometers (LTAP and TAP crystals), whereas P Kα1 was measured on a single
170 spectrometer equipped with a LPET crystal. The images were acquired in continuous stage scan
171 mode. They have a resolution of 2048 x 1536 pixel, and the dwell time was 17 ms per pixel (Fig. 6).

172 To test for the distribution of organic matter within the belemnite rostra, thin sections were
173 studied under a fluorescence microscope (Leica DM4500P) equipped with a mercury short-arc
174 reflector lamp coupled with a Leica EL6000 compact light source. We used the blue light filter set
175 producing bright green fluorescence images (filter set I3 for blue light excitation: excitation 450-490
176 nm, emission 515 nm, voltage 100-240 VAC and 50-60 Hz frequency; Fig. 7). Fluorescence microscopy
177 in the manner applied here is an optical tool to qualitatively document the spatial distribution of
178 organic matter in shells. Fluorescence reflects organic matter and less commonly crystal lattice
179 defects and solid inclusions in crystals. Further details of this method have been presented by
180 Wanamaker et al. (2009) and Ritter et al. (subm.).

181 Confocal laser fluorescence microscopy (CLFM) images on an uncoated *Megateuthis* mount
182 were made using a Bio-Rad MRC-1024 scanning confocal microscope at the W. M. Keck Laboratory

for Biological Imaging at UW-Madison (Fig. 8). The microscope was operated with a 40 mW laser at wavelengths of 488 nm, 568 nm, and 647 nm. All three wavelengths were simultaneously rastered across the sample. Naturally occurring compounds within the sample caused fluorescence at multiple wavelengths. Images were collected through the following three emission filters: visible green light (λ = 505 to 539 nm); visible red light (λ = 589 to 621 nm); and far-red light (λ = 664 to 696 nm).

In order to analyze the three dimensional filigree framework, synchrotron radiation based micro-computed tomography was applied (Fig. 9). Data were collected at the bending magnet beam line 2-BM at the Advanced Photon Source, Argonne National Laboratory, USA. A double multilayer monochromator of 1.5% band-width provided 27.2 KeV X-rays. Images were collected in transmission mode by a CCD camera behind the sample in the hutch configuration. The sample-detector distance was set to 300 mm to collect quantitative phase contrast data. 1440 projections were acquired while the sample was rotated over 180° in steps of 0.125°. A microtomographic data set with a size of 2048 x 2048 x 1948 voxels was reconstructed using a phase retrieval algorithm (Mokso et al., 2013).

3. Results

3.1 Optical-, cathodoluminescence-, fluorescence-, and confocal laser fluorescence microscopy (TL, CL, FL, CFLM)

Under transmitted light (TL), thin sections of rostra cut perpendicular to the c-axis of calcite fibres reveal a banded distribution of calcite fibres containing brownish triangular elements of variable size (Fig. 5A, D). Some of the larger fibres contain a triangular, organic-rich centre, with its innermost domains occluded by translucent calcite. Bundling of neighbouring calcite fibres is indicated by their subparallel orientation of their a-axis (Fig. 5D). A uniform extinction (orientation) pattern of adjacent fibres under crossed polarizers is observed (Fig. 5B, E) and is in agreement with EBSD data (Fig. 4A). Individual fibres display an undulatory extinction (converging or diverging c-axes)

under crossed polarizers. Calcite occluding space between organic-rich elements and fibre reinforcement is translucent and contains little or no organic matter (Fig. 5D). Brownish, triangular elements have a relatively low optical relief, compared to the surrounding translucent calcite with a relatively higher optical relief (supplement Fig. 1A-B).

Three different luminescence patterns are observed under the cathodoluminescence microscope (CL): (i) A light blue luminescence of the brownish, triangular elements (Fig. 5C, F); (ii) dark blue, intrinsic luminescence of the translucent phase; (iii) locally, orange to red luminescent fractures and microstylolites are observed. In rare cases, fractures retrace the triangular outline of a fibre (Fig. 5C, F, supplement figure 1D).

Brownish triangular areas under transmitted light display light green fluorescence while the translucent areas show a dark green fluorescence under the fluorescence microscope (FL). Microfractures are darker under transmitted light compared to the triangular elements and show a light green fluorescence (Fig. 7A-B).

Different fluorescence patterns under the CLFM reveals calcite domains visible in BSE (and other) imaging techniques (Figs. 3, 5-7). Filled cracks fluoresce brightly in green and red wavelengths (Fig. 8B-C). Domains that are dark in BSE do not fluoresce in CLFM (Fig. 8A-D). Bright domains in BSE fluoresce brightly in CLFM at all wavelengths observed (Fig. 8A-D). Higher magnification reveals brighter fluorescence between adjacent domains that appear bright in BSE (Fig. 8D).

3.2 Scanning-electron microscopy equipped with a backscatter detector (SEM BSD)

Images collected with the scanning electron microscope equipped with a backscatter detector present important evidence for the presence of two calcite phases (dark and bright) of different chemical compositions building the rostra studied. The brownish triangular areas under transmitted light are dark in BSE. Thin sections cut perpendicular to the c-axis of the radiaxal fibrous calcite (Fig.

232 1D I-IV) reveal a complex framework, dark in BSE, surrounded by relatively brighter calcite (Figs. 1-3).
233 Cross sections of the majority of fibres are polygonal or, less often, honeycomb shaped with a tri-
234 radial (120°) symmetry representing an ultrastructure that has not been described in previous studies
235 (Figs. 1C-G, 3A-E). Individual fibre diameters vary between 10-80 µm. Calcite fibres terminate at
236 individual concentric growth layers that also form the nucleation site for the overlying, next fibre
237 generation, displaying increasing thicknesses and occurring in increasing numbers towards the outer
238 portions of the rostrum (Fig. 1A-D). Brighter area in BSE are more likely to be composed of near-
239 stoichiometric $CaCO_3$ with higher average atomic masses (mainly Ca), whereas excess C, P, Mg, or S
240 will lower the average atomic mass. Accordingly, areas with decreasing amount of Ca and increasing
241 amounts of C, P, Mg or S are darker.

242 Four section planes are presented to describe the intricate bio-composite mineral present
243 within a single fibre. The following description distinguishes between the darker framework (i), i.e.,
244 micrometre-thick branches terminating in wall-like reinforcements and (ii) tri-radial central portions;
245 and brighter fabric (iii) consisting of calcite crystals forming isopachous cement layers with individual
246 crystallites coated by submicrometre thick layers of matter darker in BSE (Fig. 1G). In all sections, we
247 observed isopachous calcite crystals oriented perpendicular to the inner dark walls (Fig. 3A-E).
248 Section plane I consists of three simple, dark in BSE branches of variable lengths. Often, these
249 branches exhibit reinforcements of variable lengths and thicknesses (about 1 micrometre) and
250 increasing widths towards neighbouring branches (Figs. 1D-I, 3A). Conversely, reinforcements being
251 connected to neighboring triangles are rarely observed. Section type II is characterized by an
252 enlarged, dark in BSE central element of variable diameter (2-30 µm, Figs. 1D-II, 3C). Some of the
253 larger central elements display an inner zone with additional tri-radial structures comprising of
254 smaller, isopachous, brighter in BSE area calcite crystals rotated by 60° relative to outer branches
255 (Figs. 1D-III, 3D; section type III). Section type IV represents the most complex fabric. Here, the inner
256 portions of larger central elements display alternating darker and brighter in BSE areas (Figs. 1D-IV,

257 3E). Generally, enlarged central elements correlate with a shortening of corresponding, darker
258 branches.

259 Thin sections cut parallel to the c-axis of the radiaxial fibrous calcite reveal an framework dark in
260 BSE of triangular shaped elements with their tips pointing towards the outer margin of the rostrum
261 (Fig. 1C-D, supplement Fig. 2). Lighter and darker areas within a single calcite fibre show their
262 composite nature. Lighter and darker areas within concentric growth rings, as visible in transmitted
263 light, depend on the number and size of these elements. Higher magnification reveals a homogenous
264 central portion ("trunk" – white line) of pyramidal morphology dark in BSE surrounded by inclined
265 isopachous calcite crystals coated by material dark in BSE. This overall pattern results in a "Christmas
266 tree like" structure (Fig. 3F). The dark framework forms the substratum upon which an isopachous,
267 translucent calcite phase nucleated (Fig. 1D, G 2-3). The boundary surface between the framework
268 dark in BSE and the surrounding carbonates brighter in BSE is, in places, corroded and uneven (Fig.
269 2).

270

271 *3.3 Electron microprobe analysis (EMPA)*

272 The contrasting chemical composition of the two different calcite phases building these rostra is
273 also revealed by EMP data. Detailed WDS scans show that the strongest variability is displayed by
274 Mg, P, and S, whereas other elements are almost constant or present in amounts close to the
275 detection limit (e.g., SrO = 0.1-0.2 wt.%; FeO = <0.1 wt.%; MnO < 0.5 wt.%. X-ray element distribution
276 maps show a generally low concentration of the elements Mg (MgO = 0.3-0.4 wt.%), P (P_2O_5 = 0.1-0.2
277 wt.%), and S (SO_3 = 0.20-0.50 wt.%). The Mg- and P-content is slightly elevated in the darker,
278 triangular areas in BSE images (MgO up to 0.6 wt.%; P_2O_5 up to 0.25 wt.%) compared to the relatively
279 brighter areas in BSE images in the centre of larger tetrahedrons and their vicinity. Lowest Mg
280 concentrations were found along microfractures that display bright luminescence colours (MgO < 0.2
281 wt.%; Fig. 6B). Sulfur has a higher concentration in the brighter areas in BSE images (SO_3 up to 0.65

282 wt.%) and lower concentrations in the darker areas in BSE images (SO_3 = 0.20-0.50 wt.%; Fig. 6D). For
283 better comparison with BSE images from other samples and with the element distribution, BSE data
284 were obtained for the same field of view (Fig. 6A).

285

286 *3.4 Electron Backscattered Diffraction imaging (EBSD)*

287 Electron backscattered diffraction was used to document the biological controlled (sensu
288 Lowenstam and Weiner, 1989; Dupraz et al., 2009; Weiner and Addadi, 2011) formation of what is
289 here assumed to represent the primary biogenic skeletal carbonate. EBSD reveals a very low
290 variation of c-axes orientation of calcite fibres (Fig. 4A). The sub-parallel orientation of the c-axes
291 {001} is documented by their close fitting in the lower hemisphere of a Schmidt net (Fig. 4E, left plot).
292 A different characteristic is found for the crystallographic orientation of the a-axes {010} of calcite
293 fibres (Fig. 4E, right plot). All a-axes are aligned along a great circle whilst the colour code of the
294 according fibres is indicative of an arrangement in bundles. Adjacent fibres (10 to 100 fibres) share a
295 similar - if not identical - orientation (Fig. 4A-B). The majority of fibre bundles are characterized by
296 blue, green and red colour coding. Specifically, the spatial orientation of individual a-axes within a
297 single fibre bundle deviates by 20° or less from the bundle mean value. Variation in the orientation of
298 the c-axis of a single calcite fibre in the range of 1-3° was observed (Fig. 4D). As the angular
299 resolution from blue to red rainbow colour shown in EBSD maps (Fig. 4A-B) has a resolution of 50°,
300 minor angular deviations (<1°) are not visible in Fig. 4A-B.

301

302 3.5 *Synchrotron radiation based micro-computed tomography (SRμCT)*

303 Tetrahedral structures are visible in three dimensions in the tomographic dataset despite the
304 high signal to noise ratio and artefacts. There is a distinct difference in X-ray attenuation between the
305 inner tri-radial elements and the surrounding calcite.

4. Interpretation and Discussion

4.1 Reconstruction of the primary belemnite rostrum ultrastructure

Data presented here document a repeated pattern of triangular elements that seem to be originally connected, building a concentric layered, highly complex, and porous framework. The space between the former skeletal elements is interpreted as pore space probably filled by body fluids or organic material during the life time of these organisms. The latter assumption is based on analogous observations in the porous endoskeletons of recent *Sepia* (Sherrard, 2000; Guerra, 2006). Referring to the high porosity observed in both, the belemnite rostrum and the sepiid cuttlebone, it is important to note that these structures are not homologous (Fuchs 2012).

Accordingly, the belemnite rostra originally consisted of an organic-rich biogenic framework of calcitic tri-radial tetrahedrons (triangular pyramids arranged perpendicular to the concentric layers during lifetime). Tetrahedrons are elongated along their c-axis with the tip of the pyramid pointing towards the precipitation site i.e., in growth direction towards the outer margin of the rostrum (Fig. 1C-D). Individual branches protruding from the edges of the tetrahedrons possess outer reinforcements acting as stabilizers. The central portion of the tetrahedrons may yield a channel-like cavity (Fig. 1D III-IV). Organic membranes at which nucleation of the tetrahedrons may have started and stopped are not preserved. However, it seems likely that such membranes were present because the bases of the tetrahedrons follow a concentric layer. Structurally, the bundling of the tri-radial elements forms a simple honeycomb-like framework in which the terminations of branches of adjacent elements are connected. The mechanical stability of the honeycomb structure is enhanced by reinforcement walls (Figs. 1D, G, 3C).

Based on the variable dimensions of skeletal elements seen in thin sections, intra-rostral pore space was visually estimated to range between 50-90% of the total rostrum (Fig. 3A: 90% pore space and 10% skeletal elements; Fig. 3B; 50% pore space and 50% skeletal elements). In this context, the

observation that pore space is not limited to the apical line region but is present across the bulk rostrum is important. The secretion of a porous, but mechanically stable orthorostrum is probably best seen in the context of a considerable reduction of energy and building material required to form this structure compared to a massive endoskeleton (Sherrard, 2000). Strict biological control, i.e. in the presence of organic templates (Chateigner et al., 2000; Richter et al., 2011), over the precipitation of primary skeletal elements is demonstrated by a systematic arrangement of adjacent elements into bundles of similar or identical orientation of their crystallographic a-axes. This configuration results in a much higher mechanical load capacity and torsion stiffness of the framework of the rostrum.

Alternating concentric Ca-rich (brighter; laminae obscurae) and C-rich layers (darker; laminae pellucidae) of Müller-Stoll (1936) are related with the banded distribution of larger and smaller organic-rich triangular elements of the primary skeletal structure of the belemnite orthorostrum (Fig. 1D, supplement Fig. 2). These layers potentially indicate differences in calcite precipitation rates. Based on petrographic and ultrastructural evidence, the Mg and Ca elemental concentrations of the rostrum, the lack of secondary micro-dolomite, and the absence of blotchy luminescence, the widely held assumption of a primary low-Mg calcite mineralogy for the studied belemnite rostra is confirmed (see discussion in Richter et al., 2003).

4.2 Early and late diagenetic processes

The presence of a highly porous primary rostrum architecture during the life time of the belemnite organism as proposed here, is in contrast to the dense fabrics observed in rostra collected in Mesozoic sedimentary successions (Fig. 1A-B). Hence, the diagenetic pathway from porous to dense fabrics deserves attention. The marine diagenetic alteration of biominerals is initiated directly after the death of a carbonate-secreting marine organism when metabolic processes come to a halt. At this early stage, organic matter outside of the orthorostrum (i.e., the belemnite animal itself) and

358 in the pore space of rostra and between biominerals decomposes (Saelen, 1989), triggering a series
359 of complex bio-chemical processes. Essentially, decomposition of organic matter is mediated by
360 microbial activity, and given the abundance of marine microbial life, there is no reason to assume
361 that this would have been different in the case examples studied here.

362 Microbial metabolic products, the presence of microbial “mucus” (extracellular polymeric
363 substance) and charged surfaces represented by microbial bodies influence the micro-environment
364 in intra-rostrum pore space by altering the balance between more reduced and more oxidized forms
365 of carbon as previously summarized under the term “alkalinity engine” (Dupraz et al., 2009).
366 Specifically, Visscher and Stolz (2005) subdivided microbial species into 5-7 groups (“guilds”) having a
367 similar metabolism. Some of these promote carbonate precipitation (e.g., cyanobacteria, sulphate
368 reducers), whilst others favour dissolution (e.g., aerobic heterotrophs, fermenters). Dupraz et al.
369 (2009) documented that the balance of microbial metabolic activities directly influences carbonate
370 precipitation or, vice versa, dissolution. Initial microbial decomposition of organic matter may result
371 in the production of organic acids lowering the pH-values in the pore space (Berner et al., 1978),
372 enhancing intra-orthorostrum dissolution of biominerals (Fig. 2).

373 As soon as the bulk of organic matter is decomposed, alkalinity is increased due to microbial
374 metabolic products enhancing the precipitation of carbonate minerals (intrinsic
375 organomineralization) leading – in the view of the authors - to the formation of the translucent,
376 isopachous calcite crystals that occlude primary pore space in rostra (Fig. 2). Obviously, any
377 assumption regarding microbial processes in these ancient carbonates must remain speculative.
378 Nevertheless, following the basic concepts laid out in Dupraz et al. (2009), we tentatively assume
379 that a first phase of decomposition was dominated by aerobic heterotrophy, sulphide oxidation, and
380 fermentation decreasing the saturation index and resulting in the corrosion of skeletal elements in
381 the belemnite rostrum. Evidence for this comes from micro-corrosion features at the outer surfaces
382 of the primary skeletal framework forming the substratum upon which the pore-filling, secondary
383 calcite phase nucleates (Fig. 2).

384 The nucleation and precipitation of the secondary calcite phase (Fig. 1D, G, 2-3) was possibly
385 dominated by sulphate reduction increasing the saturation index and hence favoring precipitation of
386 $CaCO_3$. During crystals growth, remnants of belemnite organic matter combined with microbial
387 mucus were likely trapped between single crystals or at the growth front of crystals and delineate
388 crystal boundaries. Specifically, the growth of fibrous calcitic crystals will proceed as long as growth
389 rate, fluid supersaturation, and temperature are low enough to discourage spontaneous nucleation
390 (Oti et al., 1989). Similar processes have been described from extant echinoderm endoskeletons that
391 share a comparable amount of primary porosity with the described belemnite orthorostra (Richter et
392 al., 2003).

393 During this early stage of diagenetic evolution, the rostra most likely preserved their original
394 morphology due to the biogenic calcite framework and abiogenic calcite progressively occluding
395 former pore space preventing, in combination, a collapse of the rostra. The directly comparable, dark
396 blue intrinsic luminescence of the translucent secondary outer calcite layer and the calcite infill of
397 central pore space of many of the larger triangles (Figs. 3D-E, 5A, D, 6) suggest that both phases
398 precipitated from one fluid, or different fluids with near-identical geochemistry. This is, of course,
399 within the limitations of the geochemical resolution of the cathodoluminescence method and with
400 reference to elements that affect luminescence patterns (e.g., Mn^{2+}, Fe^{2+} and REE; see discussion in
401 Barbin 1991, 1993; Ritter et al., 2015). Conversely, the organic matter-rich triangles display a
402 moderately brighter blue luminescence pattern (Fig. 5C, F). This feature is best explained by calcite
403 lattice deformation due to the incorporation of organic matter into the crystal lattice
404 (intracrystalline) and is not necessarily indicative of a different geochemical composition. This
405 concept is supported by x-ray diffractometry (Richter et al., 2011) documenting that the fibrous
406 fabric of the belemnite rostra, lacking late diagenetic Mn-rich cements, is composed of
407 stoichiometric or near-stoichiometric calcites (d (104) = 3.030 to 3.035 Å).

408 A late diagenetic (burial) stage of rostra is documented by dissolution and compaction features
409 as indicated by microfractures and microstylolites (Figs. 2, 5C, F; Rosales et al., 2004a, b). The

410 circulation of Mn^{2+}-rich fluids caused the precipitation of a late calcite phase that occludes fractures
411 and fissures. In some cases this late phase yields a bright luminescence and is zigzag or triangular
412 shaped, tracing the morphology of the triangular biominerals (Fig. 5C).
413
414 *4.3 Implications for the function of the rostrum*
415
416 It is generally accepted that the belemnite rostrum acts as a counterweight to the soft body.
417 Based on the observation of a high primary porosity (see also Spaeth, 1971, 1973, 1975; Ullmann et
418 al., 2015), this interpretation requires renewed consideration. Rostra are commonly considered to
419 have the same density as inorganic calcite crystals, ranging from 2.5-2.7 g/cm³.
420 *Sepia*, the closest living relative of the extinct belemnites, incorporates a total of 10-40% organic
421 matter in its cuttlebone and comparably high amounts of intracrystalline organics were observed for
422 the biogenic belemnite orthorostrum. Accordingly, ignoring open pore space, a reduced density of
423 the biogenic belemnite calcite of about 2.4 g/cm³ (10% organic) – 2.0 g/cm³ (40% organic) results.
424 Assuming that liquid or extracrystalline organic matter (1.03 g/cm³) - with density comparable to that
425 of seawater (1.026 g/cm³) - filled up the pore space of living belemnite rostra, an overall density of
426 the rostrum ranging between roughly 1.7-1.1 g/cm³ (mean 1.4 g/cm³) is tentatively assumed on the
427 level of a working hypothesis. If these assumptions hold true, then the belemnite rostrum had a
428 cumulative density that is significantly lower than that of stoichiometric calcite. Therefore, questions
429 regarding the locomotion of belemnites result.
430 A possible analogue may come from a structure reported from a modern onychoteuthid squid
431 (*Onykia*) that has remarkable morphological similarity to the *Megateuthis* rostrum. *Onykia* has a
432 purely organic rostrum that due to its very low density does not act as a counterweight for the soft
433 body. It is assumed that it supports the posterior part of the mantle and fins (= axial stability in
434 Bizikov and Arkhipkin, 1997 and Arkhipkin et al., 2015). A function as a muscle attachment structure
435 for belemnite rostra was first put forward by Stevens (1965). Direct evidence for the presence of fins

436 in belemnites has recently reported by Klug et al. (2015), favouring a squid-like high speed swimming
437 mode of life for Jurassic belemnites. Noteworthy to report here, is the case of belemnites
438 (*Chitinoteuthis*) with a non-calcified rostrum (Müller-Stoll, 1936).
439
440 **5 Open questions and suggestions for future research**

441 5.1. Paragenesis of porosity-occluding calcite phase

442 Within individual belemnite rostra, data presented here differentiate: (i) a biogenic, highly
443 porous skeletal framework secreted during the life time of the organism; (ii) an inorganic or
444 organomineralic – arguably early diagenetic - calcite phase occluding the pore space of the biogenic
445 framework; and (iii) a late diagenetic, burial, Mn-rich carbonate phase filling fissures and larger
446 cracks within the rostra. Assuming that the above-discussed paragenetic succession is valid, a series
447 of open questions result. In the view of the authors, it is at least conceivable that portions of the
448 rostral pore space were occluded during the life time of the belemnites (remote biomineralization
449 sensu Hücker and Hemleben, 1976; Chinzei and Seilacher, 1993; Seilacher and Chinzei, 1993). If this
450 holds true, then the paragenetic sequence of primary framework and secondary infill calcite is even
451 more complicated than presented here and gradual in nature. Moreover, individual growth
452 increments within rostra are then not representative of specific correlative time intervals.
453 Specifically, each growth increment then represents a complex composite structure of paragenetic
454 phases representing temporally different stages in the belemnite ontogenetic cycle. Obviously, this
455 would render the interpretation of time series belemnite geochemical data difficult. Evidence against
456 a biogenic infill of the skeletal pore space by remote biomineralization sensu Seilacher and Chinzei
457 (1993), however, may or may not come from the presence of a corroded outer surface of what is
458 considered the primary skeletal ultrastructure of these rostra (Fig. 2). It seems difficult to argue that
459 intra-rostrum body fluids became corrosive at some stage during the life time of the belemnite
460 animal. Clearly, these questions require further detailed work.

461

462 *5.2 Primary skeletal ultrastructure and preservation of organic matter*

463

464 The authors acknowledge the fact that despite the very detailed information regarding the
465 belemnite ultrastructure shown here, our study lacks direct evidence for a primary biogenic origin of
466 the complex, highly porous framework and the subsequent cementation by an early diagenetic
467 calcite phase. Open questions, however, remain. Specifically, the significance of preserved organic
468 matter in the biogenic belemnite calcite deserves attention. In the following, we present several lines
469 (petrographic, optical, and geochemical data) of circumstantial evidence suggesting the presence of
470 preserved organic matter.

471 The sector-wise systematic arrangement of triangular elements - with their a-axis being
472 oriented subparallel to parallel (Figs. 3A-C, 4A-B, 5A, D) - in bundles, indicate a biologically controlled
473 origin (Lowenstam and Weiner, 1989) of these fabrics. The primary belemnite rostrum ultrastructure
474 is brownish (Figs. 5A, 7A) in thin sections under transmitted light and has a relatively low optical
475 relief. According to Ullmann et al. (2014), brownish areas in thin sections of biogenic carbonates are
476 indicative of remnant organic matter (C_{org}). Under the cathodoluminescence- and fluorescence
477 microscope, the primary filigree belemnite framework shows a light blue luminescence (CL) and light
478 green fluorescence (FL). According to Wanamaker et al. (2009) and Pérez-Huerta et al. (2008),
479 fluorescence in biominerals is triggered by organic macromolecules associated with chitin
480 polysaccharides and proteins. Dark fluorescence patterns commonly refer to portions of the skeletal
481 hardparts that are relatively depleted in organic matter. Bright green fluorescence patterns typify
482 areas with increased amount of organic matter (Wanamaker et al., 2009).

483 Primary skeletal structures display darker colours in SEM-BSE images. Electron microprobe
484 analyses revealed that the biogenic skeletal calcites contain more P and Mg but less S compared to
485 what is here considered an early diagenetic, pore-filling calcite phase. Higher concentrations of P (Fig.
486 6C) may be related to the presence of organic matter. Arguments for this have been presented by

Longinelli et al. (2002, 2003) and Gröcke et al. (2003) who found phosphate (PO_4^{3-}) of presumed biogenic origin being preferentially enriched along concentric growth rings. Generally, the phosphate concentration of ancient belemnite rostra is variable but very low (less than 0.3%) comparable to that in modern *Sepia*.

The primary filigree belemnite framework does not fluoresce under the CLFM. The factors that cause fluorescence in samples studied under the CLFM are poorly constrained (Fig. 8). Naturally-occurring organic compounds such as proteins or polysaccharides can cause fluorescence in other biogenic carbonates, including brachiopods (Pérez-Huerta et al., 2008), gastropods (Guzman et al., 2007), or cephalopods (Linzmeier et al., 2016). In modern brachiopods and *Nautilus*, portions of the exoskeletons with higher amounts of intracrystalline organic matter (Clark, 1999) appear dark under CLFM (Pérez-Huerta et al., 2008; Linzmeier et al., 2016). This pattern lends support to the argument that dark triangular areas in BSE images represent the primary biogenic skeleton and contain remnants of organic matter. Marine sediments may contain abundant humic substances resulting from the degradation of marine organic matter (Nissenbaum and Kaplan, 1972) and evidence has been presented that the sulphur content of the humic substances increases with degradation (Francois 1987). Concluding, it is here proposed that humic substances caused elevated S concentrations in the diagenetic calcite phase that occludes the skeletal pore space (Fig. 6D) and causes the CLFM fluorescence in all three wavelengths (Blyth et al., 2008; Orland et al., 2009, 2012; Fig. 8).

Similarly, microtomographic data indicate the former presence of organic matter in dark triangular areas of rostra (Fig. 9) as observed in BSE images. The brightness of a carbonate observed in CT image indicates the degree of attenuation of an X-ray passing through this material (Mobilio et al., 2015). As the inner tri-radial structures of rostra appear darker in colour relative to the calcite phase fringing these structures, we suggest that the fringing phase is made of a denser calcite phase compared to the inner structure. That observation is in line with the observation of a low optical relief of these features (supplement Fig. 1A-B).

513 The interpretation presented here with regard to belemnite rostra is arguably consistent with
514 observations of 10-40% organic matrix in the *Sepia* cuttlebone (Birchall and Thomas, 1983; Florek et
515 al., 2009). This is relevant as we suggest that the belemnite rostrum is structurally similar but not
516 homologous (Fuchs 2012) to the *Sepia* cuttlebone with regard to the primary intra-skeletal porosity.
517 Having said this, the presence of preserved organic matter in ancient biogenic carbonates
518 particularly, intra-crystalline organic matter is not uncommon (Clark, 1999, 2005). Excess carbon
519 observed for *Megateuthis* has been interpreted as evidence for a former organic matrix within these
520 low-Mg calcite biominerals (Dunca et al., 2006). Similarly, Florek (2004) argued for an excess of
521 carbon in the rostra of *Belemnopsis* and *Hibolites*. Summing up: Different lines of circumstantial
522 evidence point to the presence of remnant organic matter within biominerals. These data require
523 verification or rejection via the application of spatially highly resolved geochemical data. This work is
524 presently in progress.
525

526 **5. Conclusions**

527 Ultrastructural data documented here suggest that the calcitic rostra of Mesozoic belemnites
528 yielded 50-90% primary porosity probably filled with body fluids and/or organic matter during the life
529 time of the animal. Porosity was distributed throughout the rostrum as opposed to being limited to
530 the central apical area. The primary biogenic rostrum framework consists of triaxial branches and
531 tetrahedrons of variable size forming a honeycomb-like network. This structure arguably combined
532 mechanical stability with an energy-efficient biomineralization strategy.
533 The recognition of belemnite rostra as a highly porous structure requires a re-interpretation of
534 the function of the rostrum as counterweight to the soft body and has implications for the swimming
535 mode of belemnites. On the level of a working hypothesis, we argue that the low-porosity fabric
536 found in fossil rostra collected in outcrops worldwide is the result of a syntaxial, early diagenetic
537 cement phase that nucleated upon the surface of the biogenic framework and subsequently
538 occluded the pore space. The possibility of gradual occlusion of skeletal porosity by remote

biomineralization during later ontogenetic stages during the life of the animal is possible but seems unlikely at present.

If the here-presented concepts hold true, then these new findings have significant implications with regard to geochemical proxy data collected from fossil belemnite rostra. Specifically, the fact that rostra may consist of biogenic and abiogenic calcite phases formed at different times may explain the controversially low reconstructed seawater temperatures and the uncommonly high scatter of proxy data even from well-preserved rostra collected in the same stratigraphic interval. This is because seawater properties of surficial water masses, the habitat of nektobenthic belemnites, are recorded in the biogenic portions of the rostrum whereas the early diagenetic phase reflects cooler basinal bottom or marine pore water signatures. Findings presented here form a solid and well-constrained petrographic data set but one that must be verified by high-resolution geochemical data of all paragenetic calcite phases observed.

6. Acknowledgement

We acknowledge M. Born, S. Schremmer, and T. Seemann for technical preparation of thin- and ultra thin-sections. We thank all the private collectors that generously donated material making this study possible (H. Schwandt, P. Girod, G. Grimmberger, J. Kalbe, M. Sowiak and others). We acknowledge the comments by the two journal reviewers I. Jarvis and D. Fuchs and the editorial handling by Brian Jones.

7. References

Anderson, T.F., Popp, B.N., Williams, A.C., Ho, L.Z., Hudson, J.D., 1994. The stable isotopic records of fossils from the Peterborough Member, Oxford Clay Formation (Jurassic), UK: palaeoenvironmental implications. Journal of the Geological Society, London 151, 125-138.

564 Arkhipkin, A., Weis, R., Mariotti, N., Shcherbich, Z., 2015. "Tailed" Cephalopods. Journal of Molluscan
565 Studies 81, 345-355.
566 Barbin, V., 1991. Fluctuation in shell composition in *Nautilus* (Cephalopoda, Mollusca): evidence from
567 Cathodoluminescence. Lethaia 25, 391-400.
568 Barbin, V., 2013. Application of cathodoluminescence microscopy to recent and past biological
569 materials: a decade of progress. Mineralogy and Petrology 107, 353-362.
570 Benito, M.I., Reolid, M., 2012. Belemnite taphonomy (Upper Jurassic, Western Tethys) part II: Fossil-
571 diagenetic analysis including combined petrographic and geochemical techniques.
572 Palaeogeography, Palaeoclimatology, Palaeoecology 358, 89-108.
573 Berner, R.A., Westrich, J.T., Graber, R., Smith, J., Martens, C.S., 1978. Inhibition of aragonite
574 precipitation from supersaturated seawater: a laboratory and field study. American Journal of
575 Science 278, 816-837.
576 Birchall, J.D., Thomas, N.L., 1983. On the architecture and function of cuttlefish bone. Journal of
577 Materials Science 18, 2081-2086.
578 Bizikov, V.A., Arkhipkin, A.I., 1997. Morphology and microstructure of the gladius and statolith from
579 the boreal Pacific giant squid *Moroteuthis robusta* (Oegopsida; Onychoteuthidae). Journal of
580 Zoology 241, 475-492.
581 Blyth, A.J., Baker, A., Collins, M.J., Penkman, K.E.H., Gilmour, M.A., Moss, J.S., 2008. Molecular
582 organic matter in speleothems and its potential as an environmental proxy. Quaternary Science
583 Reviews 27, 905–921.
584 Chateigner, D., Hedegaard, C., Wenk, H.R., 2000. Mollusc shell microstructures and crystallographic
585 textures. Journal of Structural Geology 22, 1723-1735.
586 Chinzei, K., Seilacher, A., 1993. Remote Biomineralization I: Fill skeletons in vesicular oyster shells.
587 Neues Jahrbuch für Geologie und Paläontologie, Abhandlungen 190, 349-361.
588 Clark, II G.R., 1999. Organic matrix taphonomy in some molluscan shell microstructures.
589 Palaeogeography, Palaeoclimatology, Palaeoecology 149, 305-312.

590 Clark, II G.R., 2005. Organic matrix in the porifera and Cnidaria: déjà vu through a temporal
591 telescope. Geological society of America Abstracts with Program 37, 366.
592 Cochran, J.K., Landman, N.H., Turekian, K.K., Michard, A., Schrag, D.P., 2003. Paleoceanography of
593 the Late Cretaceous (Maastrichtian) Western Interior Seaway of North America: evidence from Sr
594 and O isotopes. Palaeogeography Palaeoclimatology Palaeoecology 191, 45-64.
595 Cochran, J.K., Kallenberg, K., Landman, N.H., Weinreb, D., Turekian, K.K., Beck, A.J., Cobban, W.A.,
596 2010. Effect of diagenesis on the Sr, O, and C isotope composition of Late Cretaceous Mollusks
597 from the Western Interior Seaway of North America. American Journal of Science 310, 69-88.
598 Coronado, I., Pérez-Huerta, A., Rodríguez, S., 2013. Primary biogenic skeletal structures in
599 Multithecopora (Tabulata, Pennsylvanian). Palaeogeography, Palaeoclimatology, Palaeoecology
600 386, 286-299.
601 Dunca, E., Doguzhaeva, L., Schöne, B.R., Schootbrugge, B. v.d., 2006. Growth patterns in rostra of the
602 Middle Jurassic belemnite *Megateuthis giganteus*: controlled by the moon? Acta Universitatis
603 Carolinae – Geologica 49, 107-117.
604 Dupraz, C., Reid, R.P., Braissant, O., Decho, A.W., Norman, R.S., Visscher, P.T., 2009. Processes of
605 carbonate precipitation in modern microbial mats. Earth-Science Reviews 96, 141-162.
606 Dutton, A., Huber, B.T., Lohmann, K.C., Zinsmeister, W.J., 2007. High-Resolution Stable Isotope
607 Profiles of a Dimitobelid Belemnite: Implications for Paleodepth Habitat and Late Maastrichtian
608 Climate Seasonality. Palaios 22, 642–650.
609 Florek, M., Youn, H.S., Ro, C.U., Wierzbowski, H., Osán, J., Kazimierczak, W., Kuczumow, A., 2004.
610 Investigation of chemical composition of belemnite rostra by synchrotron-based X-ray
611 microfluorescence and diffraction and electron microprobe. Journal of Alloys and Compounds
612 362, 99-106.
613 Florek, M., Fornal, E., Gomez-Romero, P., Zieba, E., Paszkowicz, W., Lekki, J., Nowak, J., Kuczumow,
614 A., 2009. Complementary microstructural and chemical analyses of *Sepia officinalis*
615 endoskeleton. Materials Science and Engineering C 29, 1220-1226.

616 Francois, R., 1987. A study of sulphur enrichment in the humic fraction of marine sediments during
617 early diagenesis. Geochimica et Cosmochimica Acta 51, 17–27.
618 Fuchs, D., 2012. The “rostrum”-problem in coleoid terminology – an attempt to clarify
619 inconsistencies. Geobios 45, 29-39.
620 Goetz, A.J., Steinmetz, D.R., Griesshaber, E., Zaefferer, S., Raabe, D., Kelm, K., Irsen, S., Sehrbrock, A.,
621 Schmahl, W.W., 2011. Interdigitating biocalcite dendrites from a 3-D jigsaw structure in
622 brachiopod shells. Acta Biomaterialia 7, 2237-2243.
623 Gröcke, D.R., Price, G.D., Ruffell, A.H., Mutterlose, J., Baraboschkin, E., 2003. Isotopic evidence for
624 Late Jurassic-Early Cretaceous climate change. Palaeogeography, Palaeoclimatology,
625 Palaeoecology 202, 97-118.
626 Guerra, A., 2006. Ecology of *Sepia officinalis*. Vie et Milieu – Life & Environment 56, 97-107.
627 Guzman, N., Ball, A.D., Cuif, J.-P., Dauphin, Y., Denis, A., Ortlieb, L., 2007. Subdaily growth patterns
628 and organo-mineral nanostructure of the growth layers in the calcitic prisms of the shell of
629 *Concholepas concholepas* Bruguière, 1789 (Gastropoda, Muricidae). Microscopy and
630 Microanalysis 13, 397-403.
631 Huber, B.T., Hodell, D.A., 1996. Middle-Late Cretaceous climate of the Southern high latitudes: Stable
632 isotopic evidence for minimal equator-to-pole thermal gradients: Discussion and reply.
633 Geological Society of America Bulletin 108, 1193-1196.
634 Hückel, U., Hemleben, C., 1976. Diagenetische Spurenelement-Verschiebungen und Veränderungen
635 der Skelett-Strukturen bei Belemniten Rostren. Zentralblatt Geologie und Paläontologie Teil II
636 1976, 362-365.
637 Immenhauser, A., Schöne, B.R., Hoffmann, R., Niedermayr, A., 2016. Mollusc and brachiopod skeletal
638 hard parts: Intricate archives of their marine environment. Sedimentology 63, 1-59.
639 Jarvis, I., Trabucho-Alexandre, J., Gröcke, D., Uličný, D., Laurin, J., 2015. Intercontinental correlation
640 of organic carbon and carbonate stable isotope records: evidence of climate and sea-level change
641 during the Turonian (Cretaceous). The Depositional Record 1, 53-90.

642 Klug, C., Schweigert, G., Fuchs, D., Kruta, I., Tischlinger, H., 2015. Adaptations to squid-style high-
643 speed swimming in Jurassic belemnitids. Biological Letters 12, 1-5.
644 Kozdon, R., Kelly, D.C., Kita, N.T., Fournelle, J.H., Valley, J.W., 2011. Planktonic foraminiferal oxygen
645 isotope analysis by ion microprobe technique suggests warm tropical sea surface temperatures
646 during the Early Paleogene. Paleoceanography 26, 1-17.
647 Li, Q., 2011. Belemnite Palaeo-proxies and Dating of Mesozoic Carbonates. Ph.D. Thesis. 1-262,
648 Department of Earth Sciences, Univeristy College London.
649 Li, Q., McArthur, J.M., Atkinson, T.C., 2012. Lower Jurassic belemnites as indicators of palaeo-
650 temperature. Palaeogeography Palaeoclimatology, Palaeoecology 315, 38-45.
651 Li, Q., McArthur, J.M., Doyle, P., Janssen, N., Leng, M.J., Müller, W., Reboulet, S., 2013. Evaluating
652 Mg/Ca in belemnite calcite as a palaeo-proxy. Palaeogeography Palaeoclimatology,
653 Palaeoecology 388, 98-108.
654 Linzmeier, B.J., Kozdon, R., Peters, S.E., Valley, J.W., 2016. Oxygen isotope variability within *Nautilus*
655 shell growth bands. PLoS ONE (Accepted).
656 Longinelli, A., Iacumin, P., Ramigni, M., 2002. $\delta^{18}O$ of carbonate, quartz and phosphate from
657 belemnite guards: implications for the isotopic record of old fossils and the isotopic composition
658 of ancient seawater. Earth and Planetary Science Letters 203, 445-459.
659 Longinelli, A., Wierzbowski, H., Matteo, A. di, 2003. $\delta^{18}O(PO_4^{3-})$ and $\delta^{18}O$(CO32-) from belemnite
660 guards from Eastern Europe: implications for palaeoceanographic reconstructions and for the
661 preservation of pristine isotopic values. Earth and Planetary Science Letters 209, 337-350.
662 Lowenstam, H.A., Weiner, S., 1989. On Biomineralization. Oxford University Press, New York 324 pp.
663 Lukeneder, A., Harzhauser, M., Müllegger, S., Piller, W.E., 2010. Ontogeny and habitat change in
664 Mesozoic cephalopods revealed by stable isotopes ($\delta^{18}O$, $\delta^{13}C$). Earth and Planetary Science
665 Letters 296, 103-114.

Massonne, H.-J., Neuser, R.D., 2005. Ilmenite exsolution in olivine from the serpentinite body at Zöblitz, Saxonian Erzgebirge – microstructural evidence using EBSD. Mineralogical Magazine 69, 119-124.

McArthur, J.M., Janssen, N.M.M., Reboulet, S., Leng, M.J., Thirlwall, M.F., Schootbrugge, B. v.d., 2007. Palaeotemperatures, polar ice-volume, and isotope stratigraphy (Mg/Ca, $\delta^{18}O$, $\delta^{13}C$, $^{87}Sr/^{86}Sr$): The Early Cretaceous (Berriasian, Valanginian, Hauterivian). Palaeogeography Palaeoclimatology, Palaeoecology 248, 391-430.

Mobilio, S., Boscherini, F., Meneghini, C., 2015. Synchrotron Radiation: Basics, Methods and Applications. Springer Berlin Heidelberg.

Mokso, R., Marone, F., Irvine, S., Nyvlt, M., Schwyn, D., Mader, K., Taylor, G.K., Krapp, H.G., Skeren, M., Stampanoni, M., 2013. Advantages of phase retrieval for fast X-ray tomographic microscopy. Journal of Physics D: Applied Physics 46, 1-12.

Müller-Stoll, H., 1936. Beiträge zur Anatomie der Belemnoidea. Nova Acta Leopoldina-Abhandlungen der Kaiserlich Leopoldinisch-Carolinisch Deutschen Akademie der Naturforscher, Neue Folge 4, 1-70.

Neuser, R.D., Bruhn, F., Götze, J., Habermann, D., Richter, D.K., 1996. Kathodolumineszenz: Methodik und Anwendung. Zentralblatt Geologie und Paläontologie Teil 1 1995, 287-306.

Niebuhr, B., 1995. Fazies-Differenzierungen und ihre Steuerungsfaktoren in der höheren Oberkreide von S-Niedersachsen/Sachsen-Anhalt (N-Deutschland). Berliner Geowissenschaftliche Abhandlungen, Reihe A 174, 1-131.

Niebuhr, B., Hiss, M., Kaplan, U., Tröger, K.A., Voigt, S., Voigt, T., Wiese, F., Wilmsen, M., 2007. Lithostratigraphie der norddeutschen Oberkreide. Schriftenreihe der Deutschen Gesellschaft für Geowissenschaften 55, 1-136.

Nissenbaum, A., Kaplan, I.R., 1972. Chemical and isotopic evidence for the *in situ* origin of marine humic substances. Limnology and Oceanography 17, 570-582.

691 Orland, I.J., Bar-Matthews, M., Kita, N.T., Ayalon, A., Matthews, A., & Valley, J.W., 2009. Climate
692 deterioration in the Eastern Mediterranean as revealed by ion microprobe analysis of a
693 speleothem that grew from 2.2 to 0.9 ka in Soreq Cave, Israel. Quaternary Research 71, 27–35.
694 Orland, I.J., Bar-Matthews, M., Ayalon, A., Matthews, A., Kozdon, R., Ushikubo, T., Valley, J.W., 2012.
695 Seasonal resolution of Eastern Mediterranean climate change since 34 ka from a Soreq Cave
696 speleothem. Geochimica et Cosmochimica Acta 89, 240–255.
697 Oti, M.N., Ogbuji, L.U., Breuer, K.H., 1989. Diagenetic transformation of magnesium calcite in a
698 monocrystalline rock-forming carbonate skeleton of an echinoderm. Chemical Geology 76, 303-
699 308.
700 Parkinson, D., Curry, G.B., Cusack, M., Fallick, A.E., 2005. Shell structure, patterns and trends of
701 oxygen and carbon stable isotopes in modern brachiopod shells. Chemical Geology 219, 193-235.
702 Podlaha, O.G., Mutterlose, J., Veizer, J., 1998. Preservation of $\delta^{18}O$ and $\delta^{13}C$ in belemnite rostra from
703 the Jurassic/Early Cretaceous successions. American Journal of Science 298, 324-347.
704 Price, G.D., Page, K.N., 2008. A carbon and oxygen isotopic analysis of molluscan faunas from the
705 Callovian-Oxfordian boundary at Redcliff Point, Weymouth, Dorset: implications for belemnite
706 behaviour. Proceedings of the Geologists´ Association 119, 153-160.
707 Price, G.D., Sellwood, B.W., 1997. “Warm” palaeotemperatures fron high Late Jurassic
708 palaeolatitudes (Falkland Plateau): Ecological, environmental or diagenetic controls?
709 Palaeogeography Palaeoclimatology, Palaeoecology 129, 315-327.
710 Price, G.D., Wilkinson, D., Hart, M.B., Page, K.N., Grimes, S.T., 2009. Isotopic analysis of coexisting
711 Late Jurassic fish otoliths and molluscs: Implications for upper-ocean water temperature
712 estimates. Geology 37, 215-218.
713 Price, G.D., Fözy, I., Janssen, N.M.M., Pálfy, J., 2011. Late Valanginian-Barremian (Early Cretaceous)
714 palaeotemperatures inferred from belemnite stable isotope and Mg/Ca ratios from Bersek
715 Quarry (Gerecse Mountains, Trandanubian Range, Hungary). Palaeogeography
716 Palaeoclimatology, Palaeoecology 305, 1-9.

717 Price, G.D., Hart, M.B., Wilby, P.R., Page, K.N., 2015. Isotopic analysis of Jurassic (Callovian) molluscs
718 from the Christian Malford Lagerstätte (UK): Implications for ocean water temperature estimates
719 based on belemnoids. Palaios 30, 645-654.
720 Richter, D.K., Götte, T., Götze, J., Neuser, R.D., 2003. Progress in application of cathodoluminescence
721 (CL) in sedimentary petrology. Mineralogy and Petrology 79, 127-166.
722 Richter, D.K., Neuser, R.D., Schreuer, J., Gies, H., Immenhauser, A., 2011. Radiaxial-fibrous calcites: a
723 new look on an old problem. Sedimentary Geology 239, 23-36.
724 Ritter, A.-C., Kluge, T., Berndt, J., Richter, D.K., John, C.M., Bodin, S., Immenhauser, A., 2015.
725 Application of redox sensitive proxies and carbonate clumped isotopes to Mesozoic and
726 Palaeozoic radiaxial fibrous cements. Chemical Geology 417, 306-321.
727 Ritter, A.-C., Mavromatis, V., Dietzel, M., Wiethoff, F., Griesshaber, E., Casella, L., Schmahl, W.,
728 Koelen, J., Neuser, R.D., Leis, A., Buhl, D., Niedermayr, A., Bernasconi, S.M., Immenhauser, A.
729 (submitted). Experimental diagenesis: I – Exploring the impact of diagenesis on (isotope)
730 geochemical and microstructural features in biogenic aragonite. Geochimica et Cosmochimica
731 Acta.
732 Rosales, I., Quesada, S., Robles, S., 2001. Primary and diagenetic isotopic signals in fossils and
733 hemipelagic carbonates: the Lower Jurassic of northern Spain. Sedimentology 48, 1149-1169.
734 Rosales, I., Quesada, S., Robles, S., 2004a. Paleotemperature variations of Early Jurassic seawater
735 recorded in geochemical trends of belemnites from the Basque-Cantabrian basin, northern Spain.
736 Palaeogeography, Palaeoclimatology, Palaeoecology 203, 253-275.
737 Rosales, I., Robles, S., Quesada, S., 2004b. Elemental and oxygen isotope composition of Early
738 Jurassic Belemnites: Salinity vs. Temperature signals. Journal of Sedimentary Research 74, 342-
739 354.
740 Saelen, G., 1989. Diagenesis and construction of the belemnite rostrum. Palaeontology 32, 765-798.

741 Seilacher, A., Chinzei, K., 1993. Remote Biomineralization 2: Fill skeletons controlling buoyancy in
742 shelled cephalopods. Neues Jahrbuch für Geologie und Paläontologie, Abhandlungen 190, 363-
743 373.
744 Sessa, J.A., Larina, E., Knoll, K., Garb, M., Cochran, J.K., Huber, B.T., MacLeod, K.G., Landman, N.H.,
745 2015. Ammonite habitat revealed via isotopic composition and comparisons with co-occurring
746 benthic and planktonic organisms. Proceedings of the National Academy of Sciences of the
747 United States of America 112, 15562-15567.
748 Sherrard, K.M., 2000. Cuttlebone Morphology Limits Habitat Depth in Eleven Species of *Sepia*
749 (Cephalopoda: Sepiidae). Biological Bulletin 198, 404-414.
750 Spaeth, C., 1971. Aragonitische und calcitische Primärstrukturen im Schalenbau eines Belemniten aus
751 der englischen Unterkreide. Paläontologische Zeitschrift 45, 33-40.
752 Spaeth, C., 1973. Weitere Untersuchungen der Primär- und Fremdstrukturen in calcitischen und
753 aragonitischen Schalenlagen englischer Unterkreide-Belemniten. Paläontologische Zeitschrift 47,
754 163-174
755 Spaeth, C., 1975. Zur Frage der Schwimmverhältnisse bei Belemniten in Abhängigkeit vom
756 Primärgefüge der Hartteile. Paläontologische Zeitschrift 49, 321-331.
757 Stevens, G.R., 1965. The Jurassic and Cretaceous Belemnites of New Zealand and a Review of the
758 Jurassic and Cretaceous Belemnites of the Indo-Pacific Region. New Zealand Geological Survey
759 Paleontological Bulletin 36, 1-283.
760 Swart, P.K., 2015. The geochemistry of carbonate diagenesis: The past, present and future.
761 Sedimentology 62, 1233-1304.
762 Ullmann, C.V., Korte, C., 2015. Diagenetic alteration in low-Mg calcite from macrofossils: A review.
763 Geological Quarterly 59, 3-20.
764 Ullmann, C.V., Frei, R., Korte, C., Hesselbo, S.P., 2015. Chemical and isotopic architecture of the
765 belemnite rostrum. Geochemica et Cosmochimica Acta 159, 231-243.

766 Ullmann, C.V., Thibault, N., Ruhl, M., Hesselbo, S.P., Korte, C., 2014. Effect of a Jurassic oceanic
767 anoxic event on belemnite ecology and evolution. Proceedings of the National Academy of
768 Sciences of the United States of America 111, 10073-10076.
769 Urey, H.C., Lowenstein, H.A., Epstein, S., McKinney, C.R., 1951. Measurements of paleotemperatures
770 and temperatures of the upper Cretaceous of England, Denmark, and the southern United States.
771 Bulletin of the Geological Society of America 62, 399-416.
772 Veizer, J., 1974. Chemical diagenesis of belemnite shells and possible consequences for
773 paleotemperature determination. Neues Jahrbuch für Geologie und Paläontologie,
774 Abhandlungen 147: 91-111.
775 Visscher, P.T., Stolz, J.F., 2005. Microbial mats as bioreactors: populations, processes and products.
776 Palaeogeography, Palaeoclimatology, Palaeoecology 219, 87-100.
777 Voigt, S., Wilmsen, M., Mortimore, R.N., Voigt, T., 2003. Cenomanian palaeotemperatures derived
778 from the oxygen isotopic composition of brachiopods and belemnites: evaluation of Cretaceous
779 palaeotemperature proxies. International Journal of Earth Sciences (Geologische Rundschau) 92,
780 285-299.
781 Wanamaker, A.D., Baker, A., Butler, P.G., Richardson, C.A., Scourse, J.D., Ridgway, I., Reynolds, D.J.,
782 2009. A novel method for imaging internal growth patterns in marine mollusks: A fluorescence
783 case study on the aragonitic shell of the marine bivalve *Arctica islandica* (Linnaeus). Limnology
784 and Oceanography: Methods 7, 673-681.
785 Weiner, S., Addadi, L., 2011. Crystalization Pathways in Biomineralization. Annual Review of Materials
786 Research 41, 21-40.
787 Wierzbowski, H., 2004. Carbon and oxygen isotope composition of Oxfordian-Early Kimmeridgian
788 belemnite rostra: palaeoenvironmental implications for Late Jurassic seas. Palaeogeography,
789 Palaeoclimatology, Palaeoecology 203, 153-168.

Wierzbowski, H., Joachimski, M.M., 2007. Reconstruction of late Bajocian-Bathonian marine palaeoenvironments using carbon and oxygen isotope ratios of calcareous fossils from the Polish Jura chain (central Poland). Palaeogeography, Palaeoclimatology, Palaeoecology 254, 523-540.

Wierzbowski, H., Joachimski, M.M., 2009. Stable Isotopes, Elemental Distribution, and Growth Rings of Belemnopsid Belemnite Rostra: Proxies for Belemnite Life Habitat. Palaios 24, 377-386.

Zachos, J., Pagani, M., Sloan, L., Thomas, E., Billups, K., 2001. Trends, Rhythms, and aberrations inglobal climate 65 Ma to present. Science 292, 686-693.

Figure captions

Fig. 1A-B) Structural and ultrastructural composition of belemnite rostra. *Belemnitella mucronata*, thin sections photographed under crossed polarizers. A) Cross section with pseudo-uniaxial cross indicating radially arranged calcite fibres, red box refers to C. B) Longitudinal section with central apical line and radiating fibres from the centre to the margin, stippled line refers to the position of cross section shown in A. C) Idealized bundle of calcite fibres, each fibre contains a stack of tetrahedral elements. D) SEM BSD image of the tetrahedral ultrastructure of *Megateuthis gigantea*, dashed lines (I-IV) indicate section planes and corresponding reconstructions. Primary skeletal framework is shown in blue, yellow and green whilst early diagenetic phase is shown in white and red for the crystal boundaries. The basis of tetrahedrons points toward the centre of the belemnite rostrum and its tip towards the rostrum margin i.e. the growth direction. E) Three dimensional

reconstruction of a single tetrahedron of the belemnite endoskeleton. F) Reconstruction of the complex spatial arrangement of biogenic and early diagenetic phases. Colour code in lower right. G) SEM image of a single complex tetrahedron (black line) with indication of structural elements. Primary skeletal components: br = branch, trc = triradial centre, rf = reinforcement, ic = isopachous crystallites. **(full page width; bw in print, colour in pdf)**

Fig. 2A-B) SEM BSD images of *Megateuthis gigantea*. A-B) Section perpendicular to the c-axes of calcite fibres (section plane II in Fig. 1D-II). White stippled line indicate dissolution features (early diagenetic), black stippled line indicate microstylolites. **(full page width; bw in print, colour in pdf)**

Fig. 2A-B) SEM BSD images of *Megateuthis gigantea*. A-B) Section perpendicular to the c-axes of calcite fibres (section plane II in Fig. 1D-II). Blue stippled line indicate dissolution features (early diagenetic), red stippled line indicate microstylolites. **(full page width; bw in print, colour in pdf)**

Fig. 3A-F) SEM BSD images of *Megateuthis gigantea*. A-E) Section perpendicular to the c-axes of calcite fibres. A) Triangular structures with a relatively thick outer, light grey margin of abiogenic early diagenetic cement and a small darker centre with branches giving rise to reinforcement structures representing the primary biogenic skeletal framework. B) Larger dark grey, organic rich triangular elements belonging to the biogenic skeletal framework, partly with light grey central abiogenic calcite filling of variable sizes. Branches are often short and cut off at variable distances from the centre. C) Some smaller and a few larger biogenic skeletal elements with cut off branches (lower arrow) and reinforcement structures (upper arrow). Note the variable expression of early diagenetic crystallites with sheaths of remnant organic matter. D) Close up of larger, biogenic skeletal elements and abiogenic isopachous calcites coated by remnants of organic matter within the brighter outer margin. Central portion of the biogenic skeletal elements shows abiogenic crystal; arrows point

to dissolved branches. E) Centre of biogenic skeletal element completely filled with abiogenic bright calcite leaving only a thin dark inner margin. F) Same specimen, section subparallel to the c-axes showing a homogenous central portion ("trunk" – white line) of pyramidal morphology rich in intracrystalline organic matter surrounded by inclined isopachous calcite crystals coated by remnants of organic matter. This overall pattern results in a "Christmas tree like" structure (compare with Fig. 1D). **(full page width; bw in print and pdf)**

Fig. 4A-E) *Megateuthis gigantea*, EBSD map with colour code in sections perpendicular to the c-axes of the fiber bundles. Same colours represent same crystallographic orientations. In A and B angular deviation from blue to red is up to 40°, in D angular deviation is 2°. A) Overview map showing the bundling of fibres with identical orientation of a-axes, black frame indicates area for close up in B; blue frame refers to Fig. 5A-C. B) Close up map, within one bundle blue tinted fibres are mainly neighboured by other blue fibres, red tinted fibres are surrounded by red fibres. C) Close up documenting minor angular deviation within one fibre (compare with D). D) Map of a single fibre with an angular deviation of 2° from blue to red, showing a slight systematic shift of axes orientation. E) Pole-plots of c-axes {001} and a-axes {010} from all fibres shown in A, all c-axes show nearly the same orientation while the a-axes demonstrate the bundled structure of the rostral fabric which may have improved the stability of the skeletal structure. **(full page width; bw in print, colour in pdf)**

Fig. 5A-F) Transmitted light, polarized light and cathodoluminescence. Thin section of *Megateuthis gigantea*, A-C refer to the blue frame in Fig. 4A, D-F are close ups (black frame in A) A and D) TL image perpendicular to the c-axes of calcite fibres, filigree biogenic skeletal framework is indicated by the dark tinted structures, primary porosity is represented by the abiogenic translucent calcites. Note banded distribution of calcite fibre domains relating to larger and smaller organic-rich biogenic skeletal elements, single fibres may contain a central portion of transparent calcite of varying size, bundling of adjacent calcite fibres is indicated by the same orientation of the triangles. B and E) Uniform extinction (orientation) of adjacent fibres under crossed polarizers. C and F) CL of abiogenic calcite portions show a dark blue, intrinsic luminescence (pure stoichiometric calcite), CL of the biogenic skeletal framework show light blue luminescence. **(full page width; bw in print, colour in pdf)**

Fig. 6) Electron microprobe data for *Megateuthis gigantea*. A) Overview BSE map B) Shows higher Mg concentrations within the triangular areas dark in BSE images and a lower Mg concentration in the surrounding area bright in BSE images. C) Shows higher P concentrations within the triangular areas dark in BSE images and a lower P concentration in the surrounding area bright in BSE images. D) Shows lower S concentrations within the triangular areas dark in BSE images and higher S concentrations in the surrounding region bright in BSE images. **(full page width; bw in print, colour in pdf)**

Fig. 7) Fluorescence microscope images for *Megateuthis gigantea*. A) Transmitted light shows brownish triangular structures, rich in organic matter and dark in BSE images, partly with central translucent areas (compare with Fig. 1D section plane IV, Fig. 3D, E, 5A, D). B) Shows brighter fluorescent triangular area compared to the in transmitted light translucent calcite. **(full page width; bw in print, colour in pdf)**

Fig. 8) Confocal laser fluorescence microscopy images of *Megateuthis gigantea*. A) CLFM images showing fluorescence in far-red light (λ = 664 to 696 nm). B) CLFM images showing fluorescence in visible green light (λ = 505 to 539 nm). C and D) CLFM images showing fluorescence in visible red light (λ = 589 to 621 nm). Triangular structures visible in other imaging techniques (Fig. 3, 5-7) do not fluoresce as brightly as cracks (B) or early diagenetic calcite (Fig. 3) separating the triangles (A, B, C, D). D) Higher magnification shows some brighter fluorescing calcite between the triangular elements dark in BSE images (Fig. 1, 3). Brightly fluorescent early diagenetic calcite separating triangles is enriched in S (Fig. 6). **(full page width; bw in print, colour in pdf)**

Fig. 9) Three-dimensional visualization of the filigree biogenic framework. Synchrotron radiation based tomographic visualization of a sub-volume of the rostrum of *Megateuthis gigantea*. Specimen was scanned with an isotropic voxel size of 0.74µm. A) Multi-planar image of a sub-domain of the original dataset with dimensions of 447x592x663 voxels, triangular elements dark in BSE images appear here as dark elements due to reduced densities. B-D) Volumetric renderings of the same sub-domain with variable rendering settings. **(full page width; bw in print, colour in pdf)**

Supplementary Figures

Fig. 1) Examples of the filigree framework from other belemnite species. A-B) *Gonioteuthis quadrata*, A) shows the Becke line outside of the triangular area with a relatively larger distance between the sample and objective. B) Image shows the Becke line within the triangular area while the distance between the sample and the objective was reduced, accordingly the triangular area (dark in BSE; Fig. 3) has a lower optical relief. C-D) *Belemnitella mucronata*, C) thin section under polarized light, D) same area under CL showing microfractures filled with Mn-rich calcite tracing the outline of triangular elements (encircled). **(full page width; bw in print, colour in pdf)**

Fig. 2) SEM BSD images of *Megateuthis gigantea*. A-F) Section plane parallel to the c-axes of calcite fibres. A-C) stepwise enlargement of a particular area. D-F) stepwise enlargement of a particular area. A and D give the impression of a concentric arrangement of distinct darker and brighter layers (black frames enlarged in B and E), arrow in D point to an organic rich layer (laminae obscura sensu Müller-Stoll, 1936). B and E) Allow the recognition of single darker structures of tetrahedral morphology with their tips pointing towards the outer margin of the belemnite rostrum, i.e. the growth direction (black frames enlarged in C and F). C and F) show the intricate framework of biogenic (dark) and abiogenic (light) carbonate phase within the rostrum, larger dark grey, triangular elements belonging to the biogenic skeletal framework, partly with light grey central abiogenic calcite filling of variable size. **(full page width; bw in print, colour in pdf)**

Highlights

We present well-constrained petrographic evidence for the complex primary biogenic framework of belemnite rostra.

Petrographic evidence demonstrates a high (50-90%) primary porosity for the bulk of the belemnite rostrum.

The relative proportion of biogenic skeletal framework versus abiogenic, earliest diagenetic calcite occluding the former pore space in rostra is assessed.

We discuss the timing and formation modes of pore-filling calcites.

The significance of these findings for reconstructions of marine palaeo-environments and the function of the rostrum is discussed.

Figure

Click here to download high resolution image

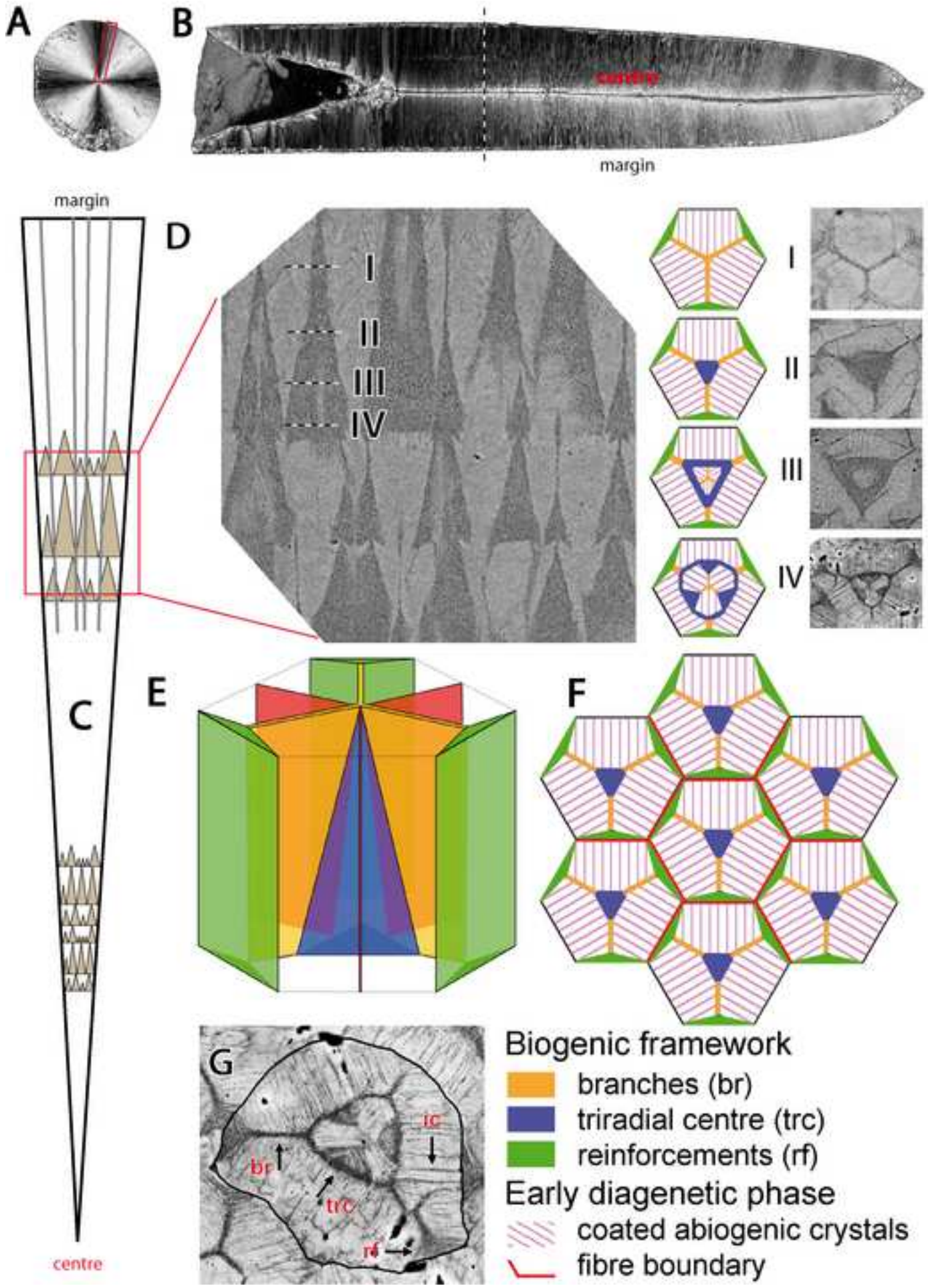

Figure
Click here to download high resolution image

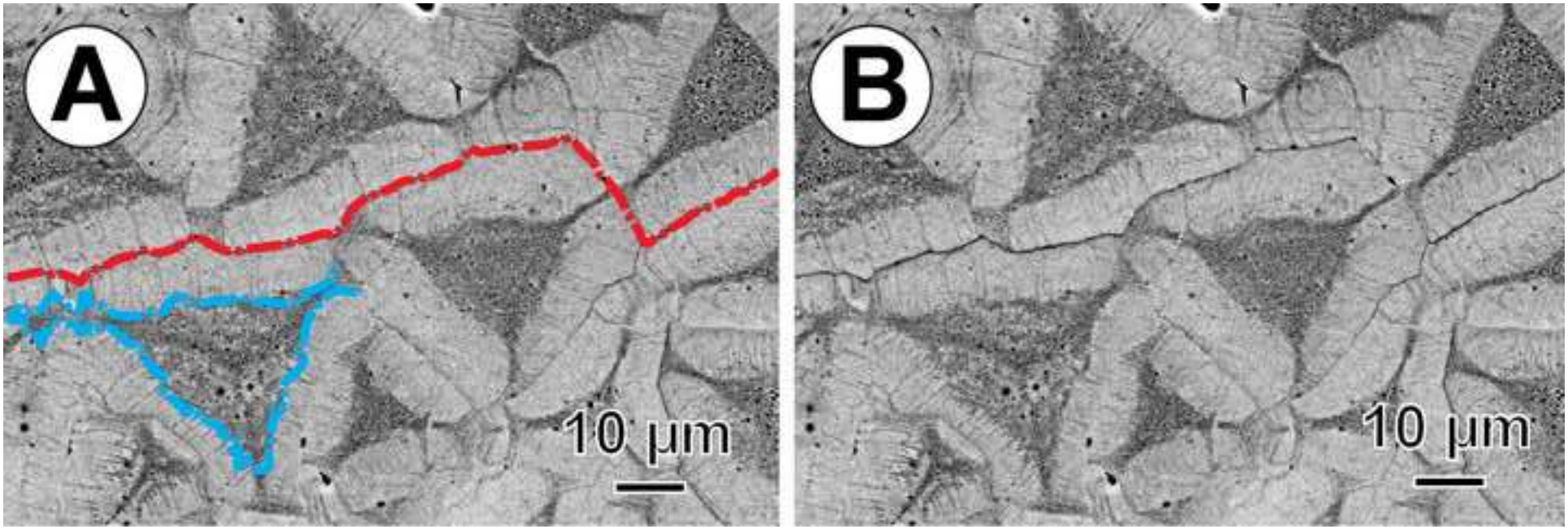

Figure

Click here to download high resolution image

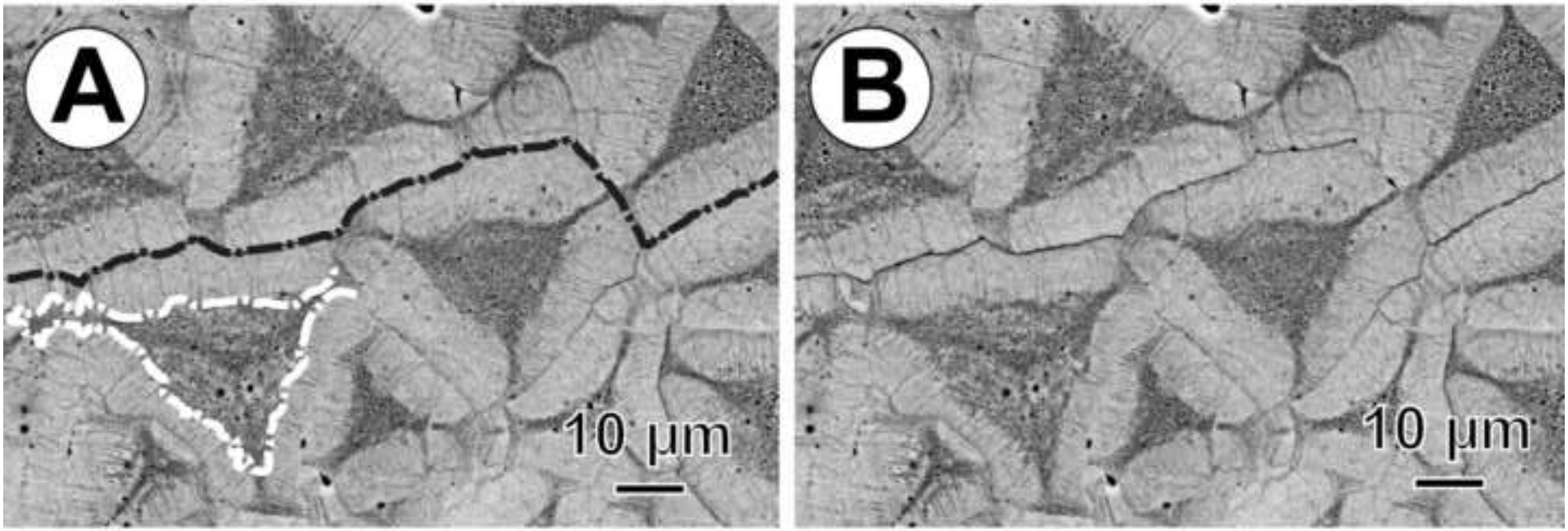

Figure
Click here to download high resolution image

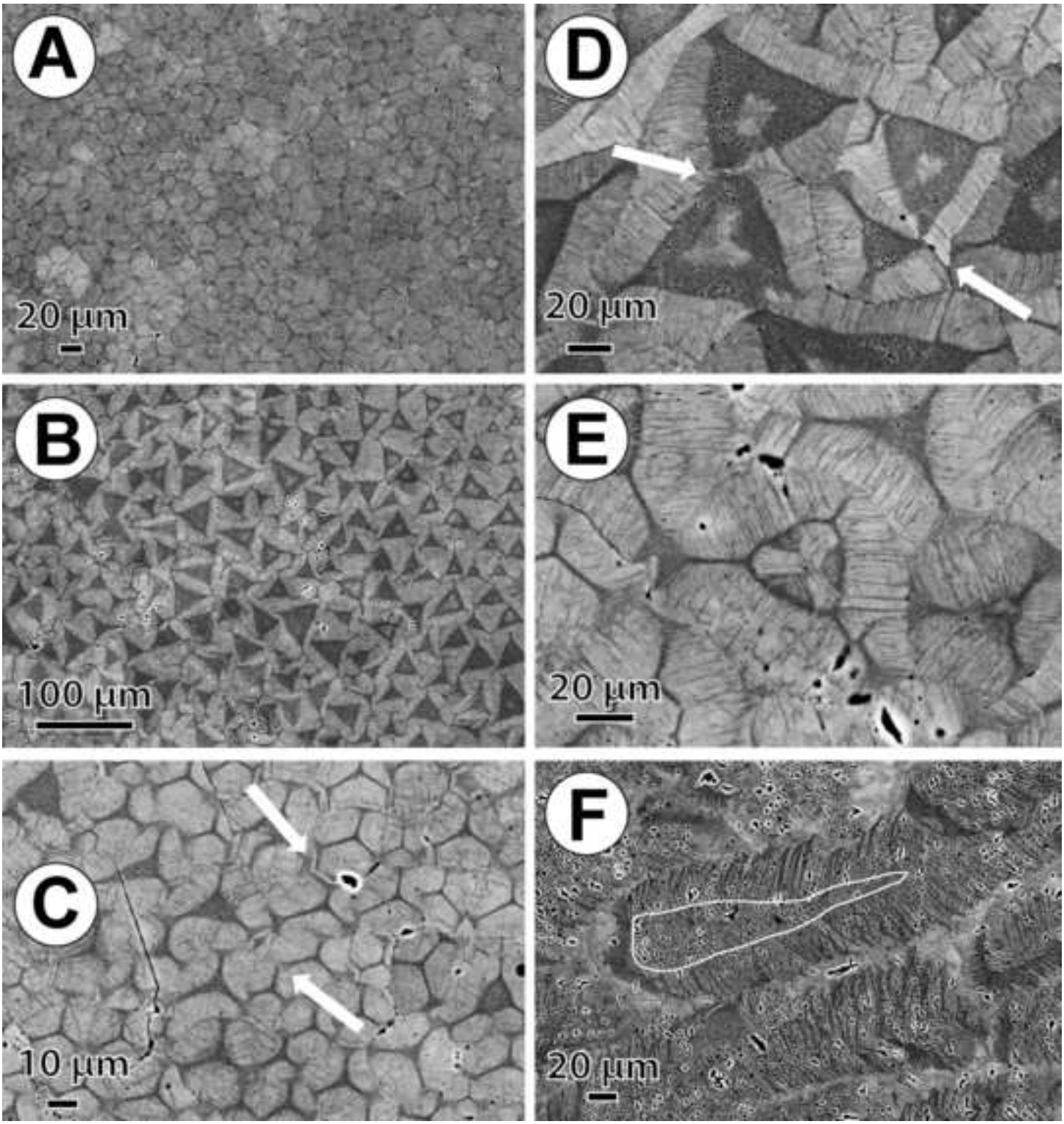

Figure

Click here to download high resolution image

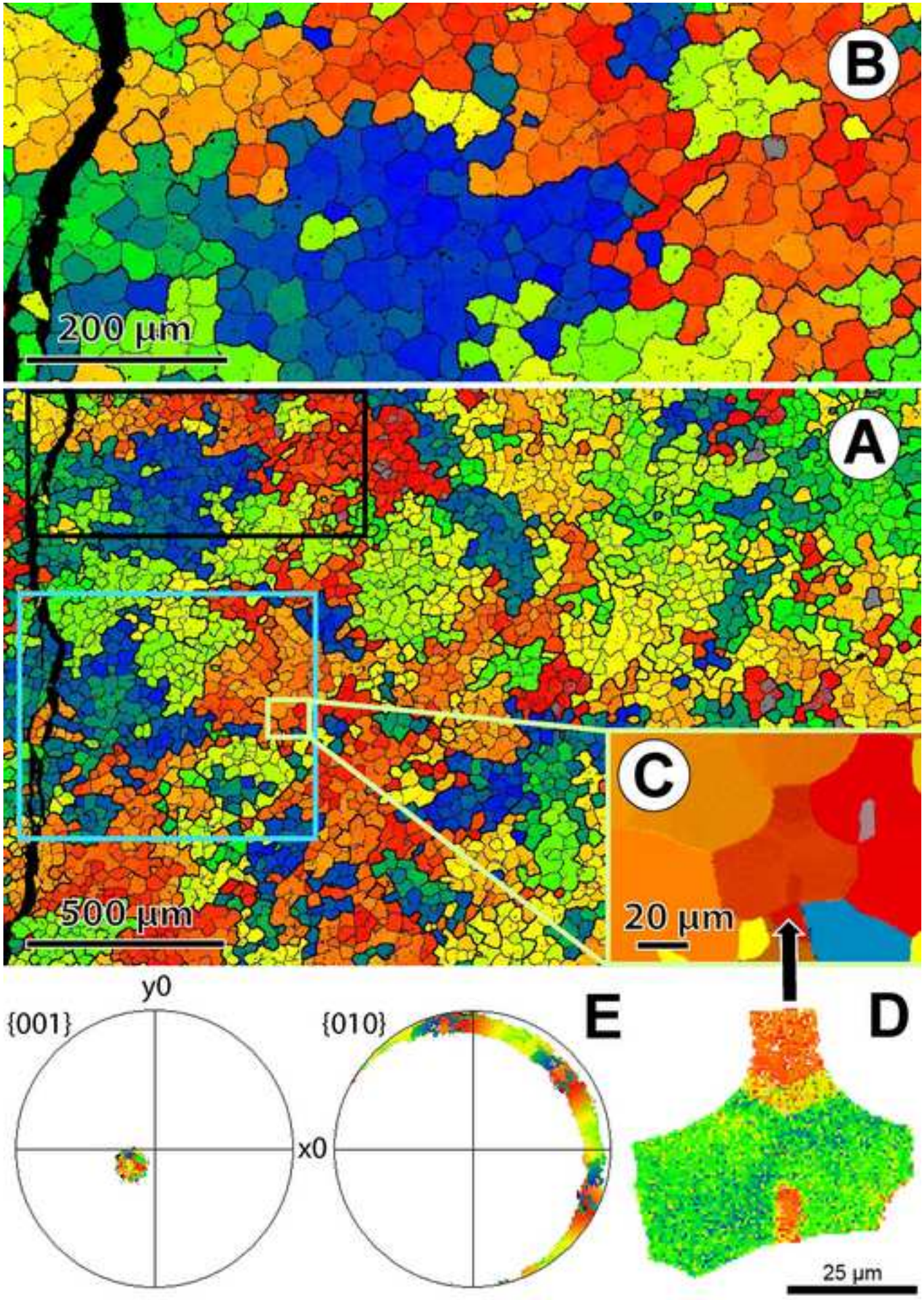

Figure
Click here to download high resolution image

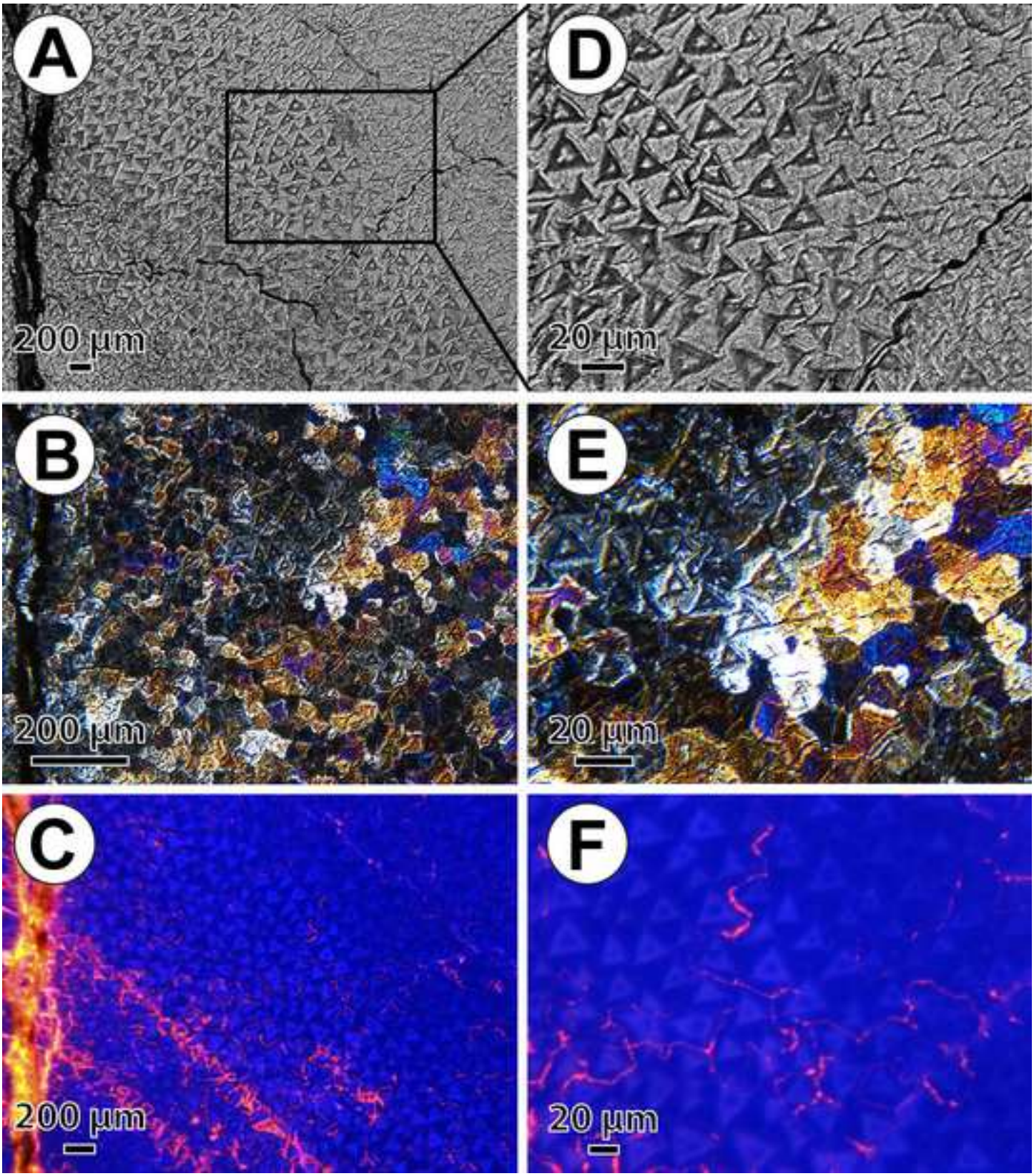

Figure

Click here to download high resolution image

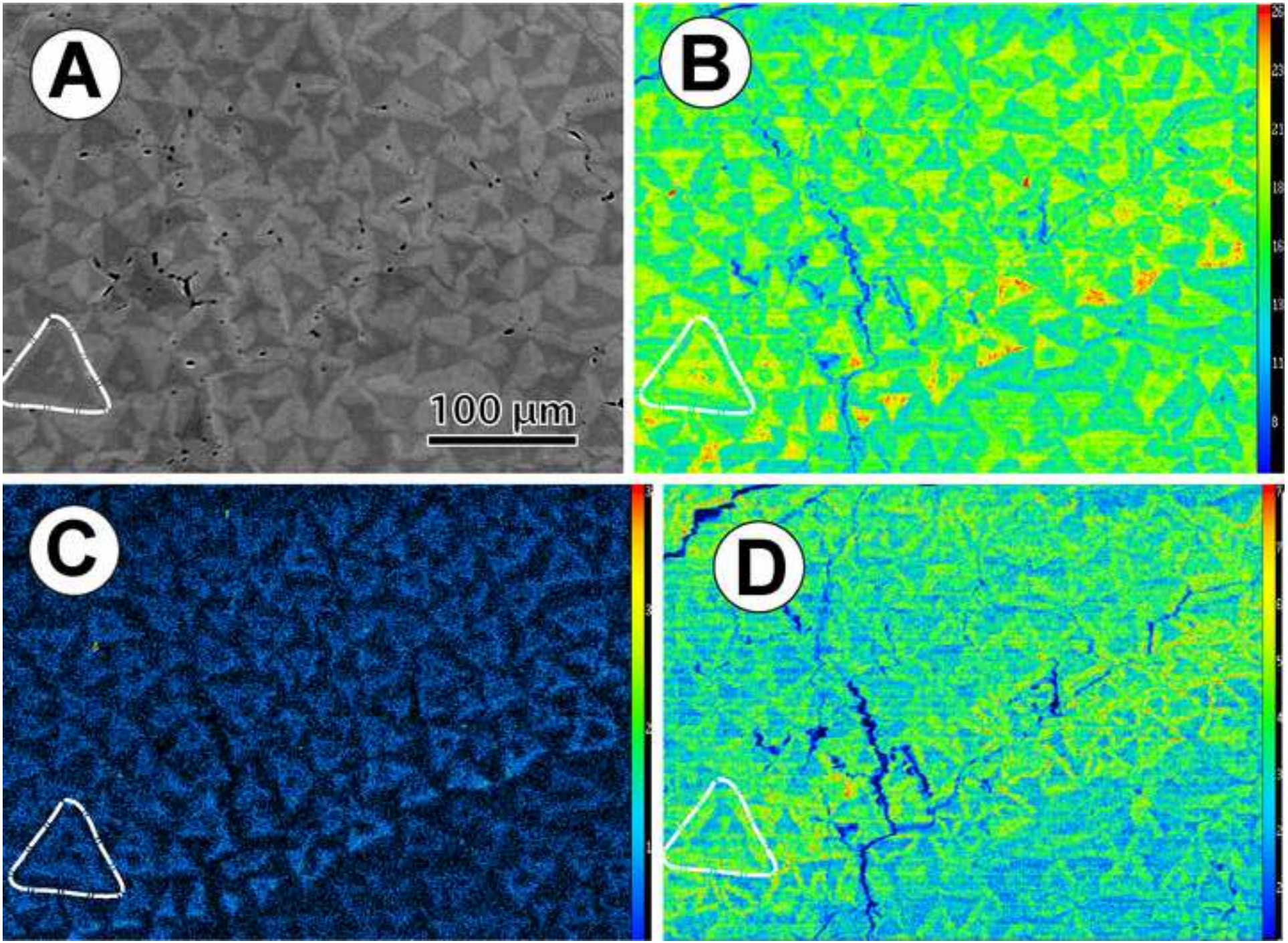

Figure

Click here to download high resolution image

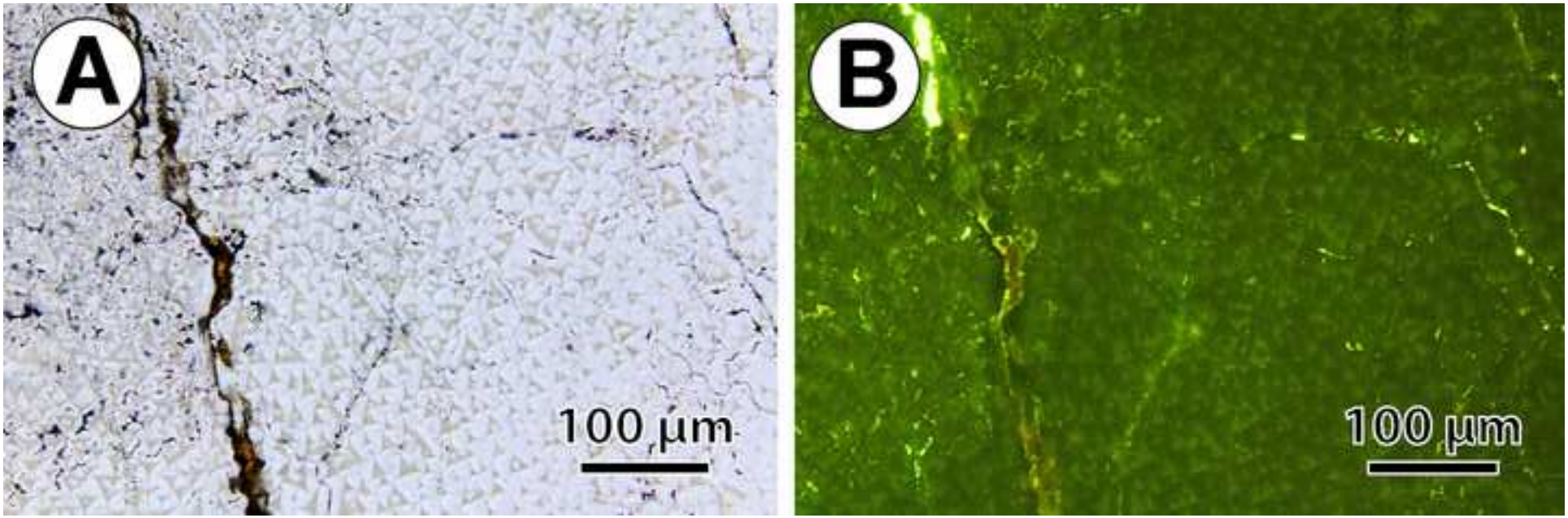

Figure

Click here to download high resolution image

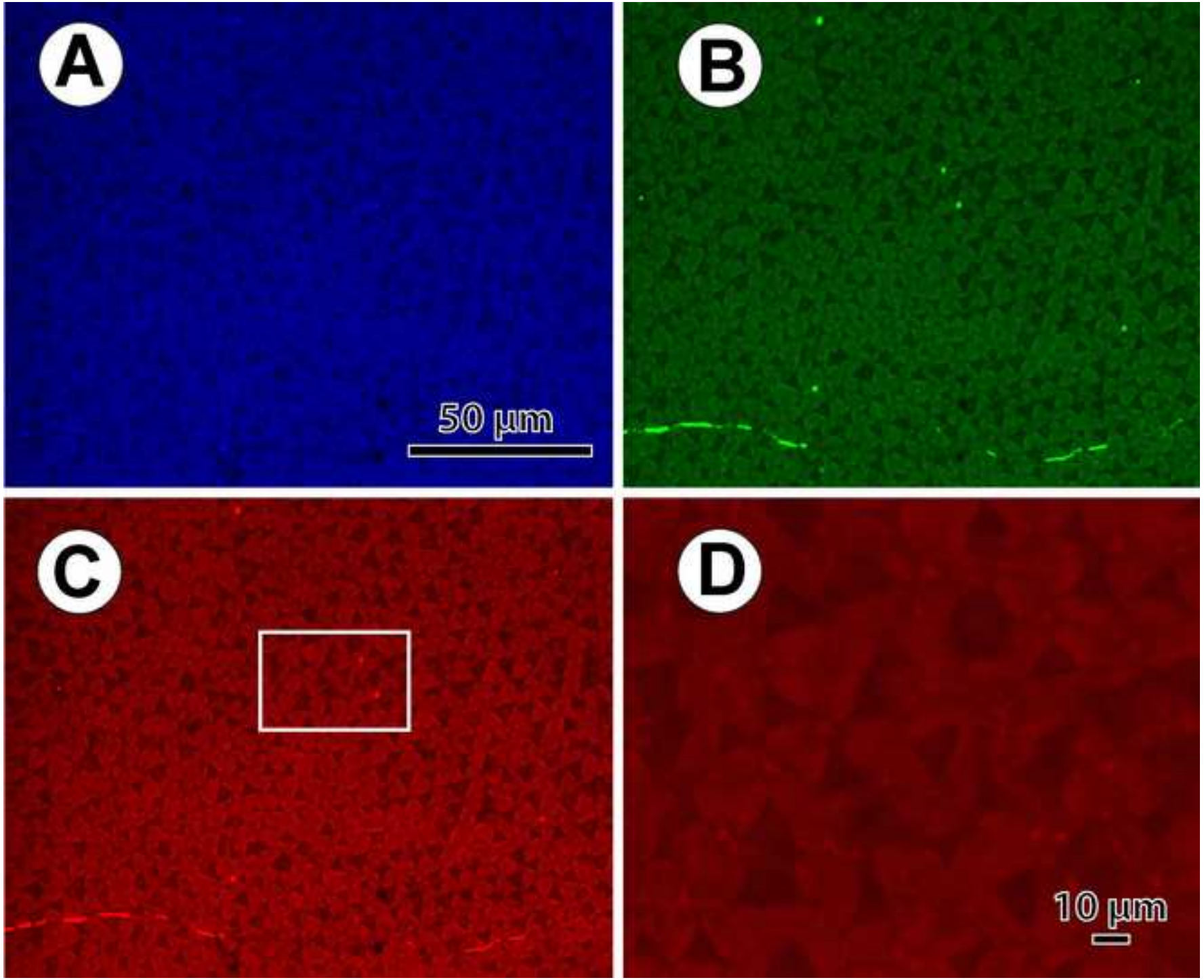

Figure

Click here to download high resolution image

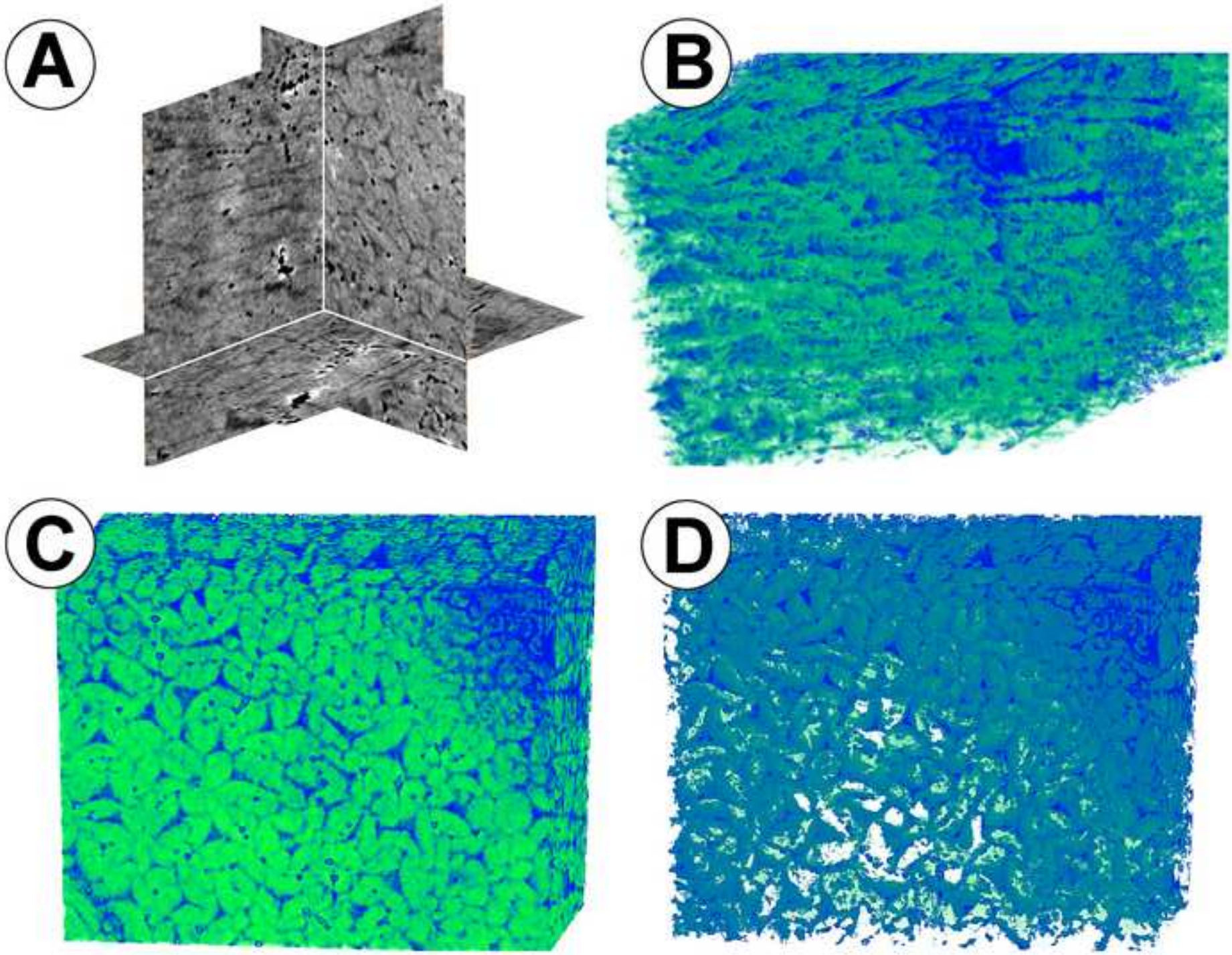

Supplementary material for on-line publication only

Click here to download Supplementary material for on-line publication only: Supplement Fig. 1 - full-width.jpg

Supplementary material for on-line publication only

Click here to download Supplementary material for on-line publication only: Supplement Fig. 2 - full width.jpg